J. Fluid Mech. (2007), *vol.* 580, *pp.* 179–217.
doi:10.1017/S0022112007005290 Printed in the United Kingdom

Inviscid and viscous aerodynamics of dense gases

PAOLA CINNELLA AND PIETRO M. CONGEDO

Dipartimento di Ingegneria dell'Innovazione, Università del Salento,
via per Monteroni, 73100, Lecce, Italy

(Received 21 February 2006 and in revised form 30 November 2006)

A numerical investigation of transonic and low-supersonic flows of dense gases of the Bethe–Zel'dovich–Thompson (BZT) type is presented. BZT gases exhibit, in a range of thermodynamic conditions close to the liquid/vapour coexistence curve, negative values of the fundamental derivative of gasdynamics. This can lead, in the transonic and supersonic regime, to non-classical gasdynamic behaviours, such as rarefaction shock waves, mixed shock/fan waves and shock splitting. In the present work, inviscid and viscous flows of a BZT fluid past an airfoil are investigated using accurate thermophysical models for gases close to saturation conditions and a third-order centred numerical method. The influence of the upstream kinematic and thermodynamic conditions on the flow patterns and the airfoil aerodynamic performance is analysed, and possible advantages deriving from the use of a non-conventional working fluid are pointed out.

1. Introduction

Dense gases are defined as single-phase vapours characterized by complex molecules and moderate to large molecular weights, operating at temperatures and pressures of the order of magnitude of those of their thermodynamic critical point. At these conditions, real gas effects play a crucial role in the dynamic behaviour of the fluid. The study of the complicated dynamics of compressible flows of dense gases is strongly motivated by the potential technological advantages of their use as working fluids in energy-conversion cycles. Specifically, such fluids possess large heat capacities compared to their molecular weight, which makes them excellent heat transfer fluids in organic Rankine cycles (ORCs). Specific interest has been developed in a class of dense gases of the retrograde type (i.e. gases that superheat when expanded), known as the Bethe–Zel'dovich–Thompson (BZT) fluids. These gases exhibit non-classical gasdynamic behaviours, such as expansion shock waves mixed shock/fan waves and splitting shocks, in a range of thermodynamic conditions above the liquid/vapour coexistence curve, such that the fundamental derivative of gasdynamics (Thompson 1971):

$$\Gamma := 1 + \frac{\rho}{a}\left(\frac{\partial a}{\partial \rho}\right)_s, \tag{1.1}$$

with ρ the fluid density, a the sound speed of, and s the entropy, becomes negative. Γ measures the rate of change of the sound speed in isentropic perturbations: if $\Gamma < 1$, the flow exhibits a reversed sound speed variation: a grows in isentropic expansions and falls in isentropic compressions, contrarily to what happens in 'common' fluids, e.g. perfect gases, for which $\Gamma = (\gamma + 1)/2$ is strictly greater than one for thermodynamic stability reasons, γ being the specific heat ratio of the fluid. The thermodynamic

region where $\Gamma < 0$ is referred to as the *inversion zone*, and the $\Gamma = 0$ contour is said to be the *transition line* (Cramer & Kluwick 1984). In flow regions with negative Γ, the second law of thermodynamics requires that compression shocks cannot form, whereas expansion shocks are physically admissible (see Cramer & Kluwick 1984). It is possible to show that the entropy change across a weak shock can be written as:

$$\Delta s = -\frac{a^2 \Gamma}{v^3} \frac{(\Delta v)^3}{6T} + O((\Delta v)^4), \tag{1.2}$$

where Δ represents a change in a given fluid property through the shock, $v = 1/\rho$ is the specific volume, and T is the absolute temperature. As a result, in order to satisfy the second law of thermodynamics, a negative change in the specific volume, i.e. a compression, is required if $\Gamma > 0$, whereas a positive change, i.e. an expansion, is the only physically admissible solution when $\Gamma < 0$. In practice, Γ rarely has constant negative sign throughout the flow, because of the finite extent of the inversion zone. At points where Γ vanishes, the genuine nonlinearity of the flow characteristic fields is lost, and non-classical waves can be generated, such as mixed shock/fan waves and splitting shocks (Cramer 1991, 1989*b*). For example, it can happen that a compressive wave would start in the positive Γ region as a shock, and then split into a compression fan as the flow enters the inversion zone. This also results in discontinuities of limited strength for thermodynamic conditions close to the transition line (Cramer & Kluwick 1984). Specifically, the shock strength is reduced up to one order of magnitude from that predicted by (1.2) for thermodynamic conditions where $\Gamma \approx 0$. A steady, inviscid dense gas flow at transonic speeds undergoing small disturbances of the speed, pressure, density, etc. is then characterized by much smaller changes of the specific entropy, and the flow can be considered, in the leading orders of the disturbances, as isentropic.

Past efforts toward demonstrating the existence of BZT fluids (see Lambrakis & Thompson 1972; Thompson & Lambrakis 1973; Cramer 1989*a*) indicate that several heavy compounds employed for heat transfer applications and as working fluids in organic Rankine power cycles (ORC) do possess BZT properties. Now, ORC turbines typically work in the transonic/low supersonic regime and their major loss mechanism is related to the generation of shock waves and their interactions with the blade boundary layers. Therefore, on the one hand a detailed study of turbomachinery flows of dense gases is necessary to predict the system behaviour correctly; on the other hand, non-classical dense gas phenomena could be exploited to improve efficiency: namely, shock formation and subsequent losses could be ideally suppressed, if turbine expansion could happen entirely within or in the immediate neighbourhood of the inversion zone. Previous works on BZT transonic flows past airfoils (Cramer & Tarkenton 1992) and through turbine cascades (Monaco, Cramer & Watson 1997; Brown & Argrow 2000) show that, properly operating the turbine in the very neighbourhood of the $\Gamma = 0$ curve, the flow field evolves almost entirely within the inversion zone and is shock-free: as a result, except for viscous drag, the flow remains almost isentropic through the entire cascade. Unfortunately, the inversion zone has a limited extent: therefore, a reduction in the temperature jump between the heater and condenser stages is generally required in order to operate the turbine completely within it. Now, it is well-known from thermodynamic theory of heat engines (see for example Cengel & Boles 2006) that too small a temperature jump implies low thermal cycle efficiency. Moreover, a small temperature (i.e. enthalpy) jump also means low cycle power output. This important drawback has been the stumbling block to the development of real-world BZT ORCs. In practice, BZT gas effects can

find application in ORC turbomachinery only if a reasonable trade-off between the above-mentioned opposite requirements is found.

Previous works on transonic dense gas flows past airfoils and through turbine cascades generally consider operating conditions in the vicinity of the transition line. Cramer & Tarkenton (1992) studied transonic flows past thin airfoils by solving an extended transonic small disturbance equation derived for flows with $\Gamma \approx 0$, $M \approx 1$ (with M the Mach number), and also characterized by small values of the second nonlinearity parameter $\Lambda := \rho(\partial\Gamma/\partial\rho)_s$ (Cramer & Kluwick 1984). They found a significant increase of the critical Mach number in flows of BZT fluids over profiles. Numerical solutions of the small disturbance equation completed by the Martin–Hou gas model revealed substantial reductions in the strength of compression shocks. Morren (1991) performed numerical simulations using the Euler equations and the van der Waals equation of state, and observed an evident decrease in the pressure drag over the airfoil. Transonic flows of a dense gas around the leading edge of a thin airfoil with a parabolic nose have been studied by Rusak & Wang (1997). Once again, the oncoming flow was supposed to be almost sonic, and characterized by small values of Γ and Λ. Asymptotic expansions of the velocity potential function were constructed in terms of the airfoil thickness ratio in an outer region around the airfoil and in an inner region near the nose. The numerical solution of the inner problem resulted in a symmetric flow around the nose, with a stagnation point located at the leading edge for every transonic Mach number and any shape and small angle of attack of the airfoil. Wang & Rusak (1999) also provided numerical studies of transonic BZT flows past a NACA0012 airfoil at zero angle of attack (non-lifting case) for oncoming flow conditions such that Γ_∞, $\Lambda_\infty \approx 0$. They developed a transonic small-disturbance solver for computing the nonlinear BZT gas flow in the outer region around most of the airfoil, while the flow in the inner region near the nose of the airfoil was computed by solving the problem of a sonic flow around a parabola. Numerical results of the composite solutions calculated from the asymptotic theory were compared with solutions of the Euler equations provided by the numerical code of Morren (1991). A discussion on the flow patterns around an airfoil at transonic speeds and various upstream thermodynamic conditions was also presented. Numerical solutions of the Euler equations for isenthalpic flows through turbine cascades by using the Martin–Hou gas model have been provided by Monaco *et al.* (1997) for incoming flow conditions characterized by small values of Γ. Numerical comparisons between BZT fluids and lighter fluids such as steam were presented, showing that BZT effects can result in significant reductions of adverse pressure gradients associated to shock wave impingement on neighbouring blades. Finally, results concerning flows through realistic impulse turbine cascades have been presented by Brown & Argrow (2000), who solved the Euler equations closed by the Martin–Hou gas model. Their results show significant improvements in turbine efficiency for BZT working fluids over conventional ones.

Cinnella & Congedo (2005*a*) have investigated the influence of BZT effects on the system performance of inviscid transonic lifting flows past a NACA0012 airfoil. Numerical simulations were performed by solving the Euler equations discretized by a third-order-accurate numerical scheme on very fine meshes. The gas response was modelled by the van der Waals equation of state for polytropic gases. In contrast with previous studies, the investigation was not restricted to flows with small free-stream Γ. On the contrary, the objective was to explore the possibility of keeping part of the benefits deriving from BZT behaviour while enlarging the operation range. To this purpose, a detailed parametric investigation of the airfoil aerodynamic performance

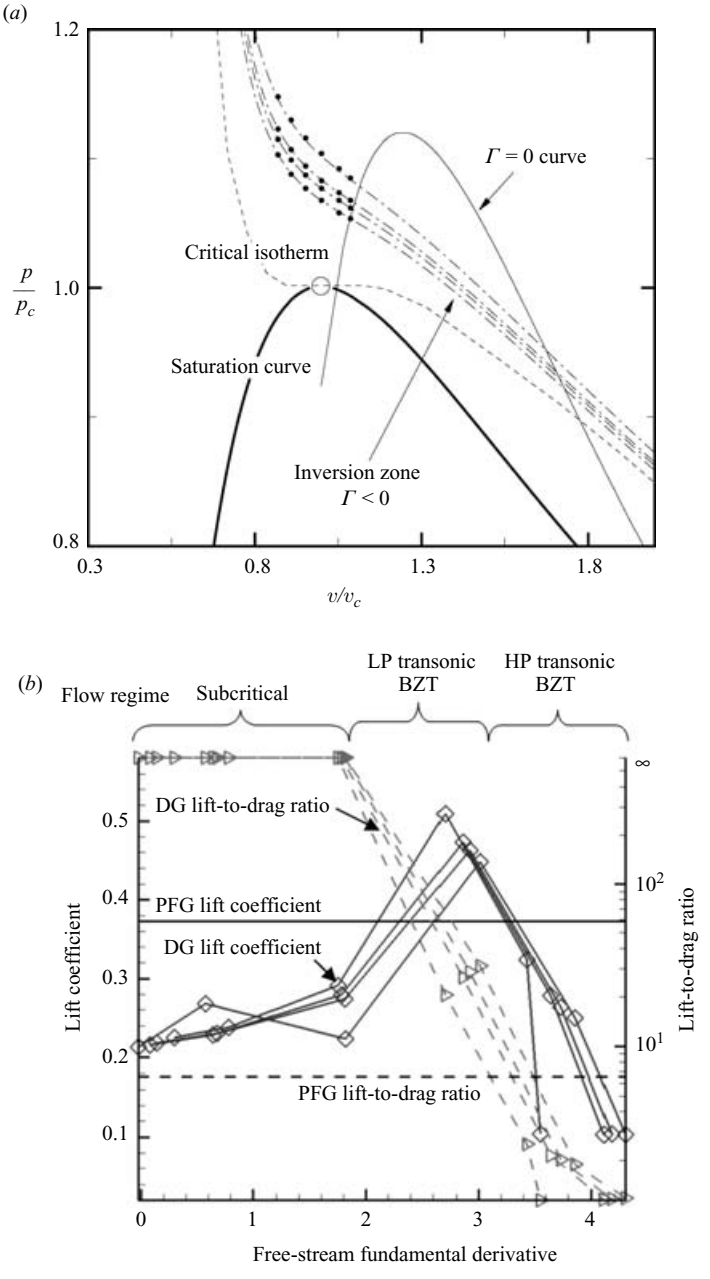

FIGURE 1. Aerodynamic performance of transonic flows at $M_\infty = 0.85, \alpha = 1^\circ$ of a BZT van der Waals gas ($\gamma = 1.0125$) past the NACA0012 airfoil. (*a*) Choice of the upstream thermodynamic conditions (black dots); (*b*) lift coefficient and lift-to-drag ratio versus free-stream fundamental derivative for a perfect gas (PFG) and for the dense van der Waals gas (DG).

was undertaken, with specific interest in configurations providing the best trade-off between high lift and low drag. Figure 1 summarizes the results obtained for a BZT van der Waals gas flowing at $M_\infty = 0.85, \alpha = 1^\circ$ over the NACA0012 airfoil for

various free-stream thermodynamic conditions, corresponding to a series of operation points selected along constant-entropy lines (isentropes) crossing the inversion zone (figure 1*a*); for each isentrope, the lift coefficient and the lift-to-drag ratio are plotted against the free-stream value of Γ (figure 1*b*). Note that the fundamental derivative does not vary monotonically along an isentrope. Nevertheless, the operating region of interest for ORCs is located at the high-pressure side of the inversion zone, where Γ monotonically increases with pressure. For the smallest values of Γ_∞, results presented in previous studies are recovered, namely, the flow is subcritical and characterized by zero drag (in the limit of vanishing mesh size). Consequently, the lift-to-drag ratio tends to infinity. The price to pay is decreased lift with respect to a system using a perfect gas as the working fluid: this is the counterpart, for an airfoil, of the aforementioned trade-off between high turbine efficiency and high cycle power output for energy-conversion systems. When Γ is sufficiently high (approximately in the range 2–3), a significant growth in both lift and drag is observed: the increase in lift is produced by the formation of an expansion shock, close to the leading edge, which strongly enhances the suction peak at the airfoil upper surface. The increase in drag is due to the occurrence of shocks on the airfoil surface. Nevertheless, losses introduced by flow discontinuities are very low, owing to the smallness of entropy changes across weak shocks in the vicinity of the transition line. In fact, the lift-to-drag ratio remains one order of magnitude greater than in perfect gas flow. Finally, when Γ_∞ reaches higher values, far from the inversion zone, the flow becomes qualitatively similar to that of a perfect gas, with even poorer performance, and the benefits due to BZT effects progressively disappear. In summary, the results presented in Cinnella & Congedo (2005*a*) suggest that the choice of upstream conditions within or very close to the transition line is not only not mandatory in order to improve airfoil performance, as suggested in previous studies, but also not optimal. Specifically, optimal aerodynamic performance (i.e. the best trade-off between high lift and low drag) is obtained for $\Gamma = O(1)$, more precisely $\Gamma \approx 3$. This is of great importance, in light of the design of BZT organic Rankine cycles, since it suggests the possibility of enlarging the operation range of the expansion stage without losing the benefits of dense gas effects.

Results presented in Cinnella & Congedo (2005*a*) have been obtained using the van der Waals equation of state, also used in many former studies, as the simplest gas model accounting for BZT effects: it is computationally inexpensive, and allows the capture of qualitative features of BZT fluid flows. On the other hand, this model is not accurate for thermodynamic conditions close to saturation, i.e. the region of interest in the present study, and largely over-predicts the extent of the inversion zone (Thompson & Lambrakis 1973). The Amagat ($p - v$) diagrams in figure 2 give an idea of the different behaviour of a polytropic van der Waals gas with $\gamma = 1.0125$, representative of a generic heavy fluorocarbon, and of a real gas modelled through the more realistic Martin–Hou equation of state, namely, the heavy perfluorocarbon pf-perhydrofluorene (commercial name PP10). The van der Waals gas exhibits a large inversion zone. Outside this zone, the fundamental derivative quickly increases, reaching values close to 3 at a short distance from the transition line, and tends to the perfect gas value when the specific volume tends to infinity. On the contrary, the inversion zone for PP10 is much smaller. Nevertheless, the increase of Γ outside the inversion zone for increasing pressure is much slower. In the following, it will be shown that this particular variation of Γ counterbalances to some extent the reduction in the inversion zone size encountered in real-world gases, and favourably affects the system performance.

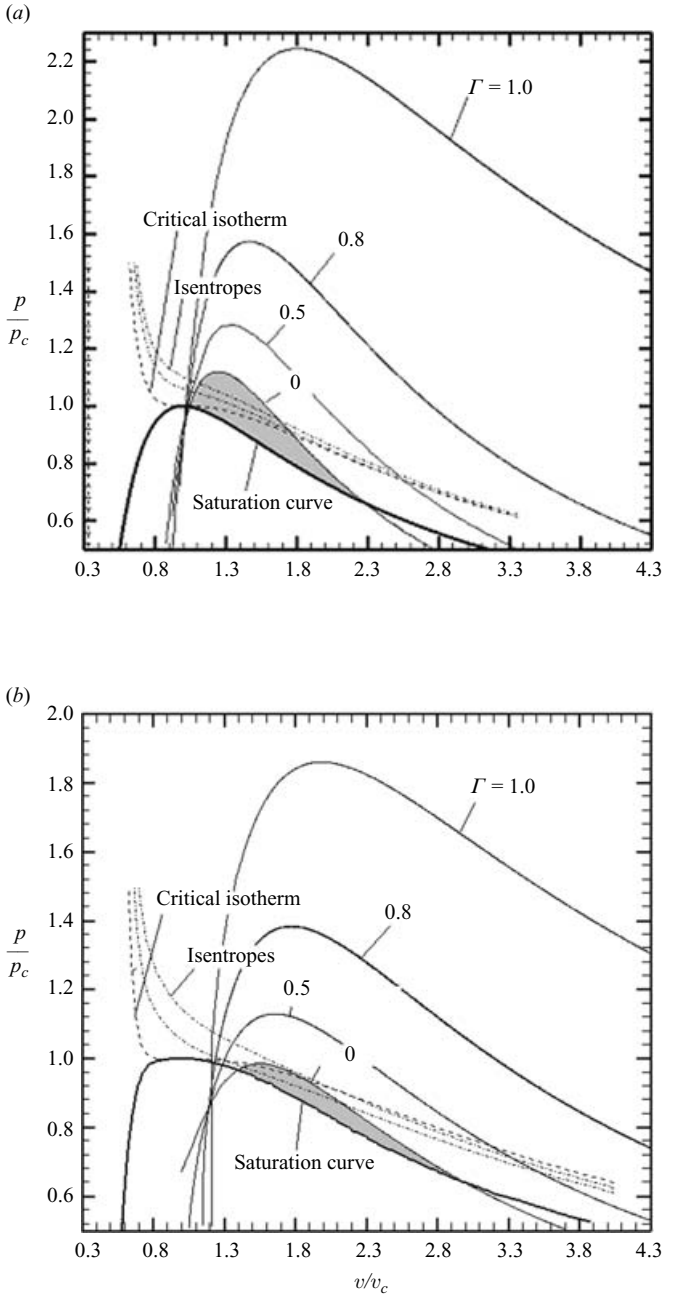

FIGURE 2. Amagat diagrams for (*a*) a BZT van der Waals gas ($\gamma = 1.0125$) and (*b*) for PP10.

Another limitation of Cinnella & Congedo (2005*a*) is related to the thermo-viscous effects being completely neglected, as in almost all previous studies. Indeed, viscous effects in flows of dense gases have remained largely unexplored. One of the most important differences between dense gases and perfect gases is the downward curvature and nearly horizontal character of the isotherms in the neighbourhood of the critical point and upper saturation curve in the (p, v)-plane: the region of

downward curvature of the isotherms is associated with the aforementioned reversed behaviour of the sound speed in isentropic perturbations. In the same region, the specific heat at constant pressure, c_p, can become quite large: this strongly influences the development of the thermal boundary layer and its coupling with the viscous boundary layer in high-speed flows. A second consideration is that in the dense gas regime, the dynamic viscosity μ and the thermal conductivity κ cannot any longer be considered independent of the temperature and pressure, even in flows with relatively small temperature variations. On the other hand, the well-known Sutherland law, commonly used to represent viscosity variation with temperature, becomes invalid, since it is based on the hypothesis that the gas molecules act as non-interacting rigid spheres, and intermolecular forces are neglected. The complexity of the behaviour of μ in the dense regime can be anticipated by recalling that the viscosity of liquids tends to decrease with increasing temperature, whereas that of gases tends to increase: the dense gas regime is a transition between these two qualitatively different behaviours. Similarly, the classical approximation of nearly constant Prandtl number ($Pr = \mu c_p/\kappa \approx \text{const}$) cannot be used any more. As the thermal conductivity has roughly the same variation as viscosity with temperature and pressure, the behaviour of Pr tends to be controlled by variations of c_p. In regions where c_p becomes large, strong variations of Pr can be observed, contrary to what happens in perfect gases. Nevertheless, if the immediate vicinity of the thermodynamic critical point is excluded from consideration, the Prandtl number remains of order one, similar to perfect gases. In contrast, the Eckert number ($Ec = U_0^2/(2\,c_p T_0)$, where U_0 and T_0 represent velocity and temperature of a suitable reference state) decreases significantly. A small flow Eckert number implies reduced sensitivity of the boundary layer to friction heating, which remains negligible even at moderately large supersonic Mach numbers.

In the past, investigations of the viscous structure of one-dimensional non-classical shocks have been presented in Cramer & Crickenberg (1991). Cramer, Whitlock & Tarkenton (1996) have presented a numerical investigation of laminar flows of dense gases over a flat plate. The results indicate a failure of classical scaling laws for compressible boundary-layers (Chapman–Rubesin scaling), and a reduction of the boundary-layer friction heating in complex gases with large heat capacities. Numerical results showing a suppression of shock-induced separation in supersonic Bethe–Zel'dovich–Thompson flows past sharp compression corners have been provided by Cramer & Park (1999). Kluwick (2000) has discussed a new form of marginal boundary-layer separation in laminar flows of dense gases using asymptotic methods: the non-monotonic Mach-number variation with pressure leads to non-conventional distributions of the shear stress and displacement body in boundary layers subjected to adverse pressure gradients, which contributes to delay separation. Kluwick & Wrabel (2004) investigated shock/boundary-layer interaction in dense gases via the triple deck theory. Their results show that it is possible to reduce the size of the separation bubble or even to avoid the occurrence of flow separation by choosing an optimal operation thermodynamic state.

In the present work, a numerical investigation of two-dimensional inviscid and viscous dense gas flows past an isolated airfoil is provided. Dense gas effects are modelled through the realistic equation of state of Martin & Hou (1955), involving five virial expansion terms. This equation is widely accepted as the reference thermodynamic model for dense gases (see for example Emanuel 1994; Guardone, Vigevano & Argrow 2004). The equation is implemented within a numerical code for dense gas flow simulations, based on a simple and efficient third-order accurate centred solver (Cinnella & Congedo 2005*b*). The code also includes proper thermophysical

models for the variation of the dynamic viscosity and thermal conductivity of dense gases (Chung *et al.* 1988). The aim of the present investigations is twofold: (i) to further investigate, using more predictive thermodynamic models, mechanisms affecting aerodynamic performance (lift, drag, lift-to-drag ratio) for inviscid dense gas flows past an airfoil, providing a more quantitative evaluation of the possible gains; (ii) to investigate for the first time, to our knowledge, how the peculiar behaviour of BZT gases affects the viscous-flow performance of an airfoil. A parametric study of the influence of free-stream thermodynamic conditions on the aerodynamic performance of BZT inviscid and viscous transonic flows past a NACA0012 airfoil has been undertaken. The results are critically analysed and compared to those obtained for a perfect diatomic gas flowing past the same configuration, pointing out peculiarities related to the use of non-conventional working fluids.

2. Governing equations and thermodynamic models

We consider the Navier–Stokes equations for compressible single-phase flows, written in integral form for a control volume Ω with boundary $\partial\Omega$:

$$\frac{\mathrm{d}}{\mathrm{d}t}\int_{\Omega} w\,\mathrm{d}\Omega + \oint_{\partial\Omega} (\boldsymbol{f} - \boldsymbol{f}_v)\cdot\boldsymbol{n}\,\mathrm{d}S = 0. \tag{2.1}$$

In (2.1), $w = (\rho, \rho\boldsymbol{v}, \rho E)^T$ (with $\boldsymbol{v}$ the velocity vector, $E = e + |\boldsymbol{v}|^2/2$ the total energy per unit mass, and e the internal energy per unit mass) is the conservative variable vector, $\boldsymbol{n}$ is the unit outer normal to Ω, and $\boldsymbol{f}$, $\boldsymbol{f}_v$ are the inviscid and the viscous part of the flux density, respectively, given by

$$\boldsymbol{f}_e = (\rho\boldsymbol{v}, \rho\boldsymbol{v}\boldsymbol{v} + p\boldsymbol{I}, \rho\boldsymbol{v}H)^T,$$

with $H = E + p/\rho$ the total enthalpy per unit mass and $\boldsymbol{I}$ the unit tensor, and

$$\boldsymbol{f}_v = (0, \boldsymbol{\tau}, \boldsymbol{\tau}\boldsymbol{v} - \boldsymbol{q})^T,$$

where $\boldsymbol{\tau} = \mu(\nabla\boldsymbol{v} + \nabla\boldsymbol{v}^T) - \frac{2}{3}\mu(\nabla\cdot\boldsymbol{v})\boldsymbol{I}$ is the viscous stress tensor and $\boldsymbol{q} = -\kappa\nabla T$ is the heat flux vector.

The equations are completed by a thermal equation of state:

$$p = p(\rho, T)$$

and by a caloric equation of state,

$$e = e(\rho, T).$$

The latter is not completely independent from the first one, since it has to satisfy the compatibility relation:

$$e = e_r + \int_{T_r}^{T} c_{v_\infty}\,\mathrm{d}T' - \int_{\rho_r}^{\rho}\left[T\left(\frac{\partial p}{\partial T}\right)_{\rho} - p\right]\frac{\mathrm{d}\rho'}{\rho'^2}.$$

In the above, $c_{v_\infty} = c_{v_\infty}(T)$ is the low-pressure, i.e. ideal gas, specific heat at constant volume, and supscript r indicates a reference state. The caloric equation of state is completely determined once a variation law for c_{v_∞} is specified. Moreover, thermodynamic models relating the dynamic viscosity, μ, and thermal conductivity, κ, to the gas temperature and pressure are required.

In the present work, the Martin–Hou thermal equation of state is used (Martin & Hou 1955), which provides a realistic description of the gas behaviour and of the

inversion zone size. Such an equation, involving five virial terms and satisfying ten thermodynamic constraints, ensures high accuracy with a minimum amount of experimental information. A power law of the form:

$$c_{v_\infty} = c_{v_\infty}(T_c)\left(\frac{T}{T_c}\right)^n$$

is used to model variations of the low-density specific heat with temperature, where n is a material-dependent parameter. The fluid viscosity and thermal conductivity are evaluated using the method proposed in Chung *et al.* (1988). The same model has also been used in Cramer *et al.* (1996) and Cramer & Park (1999)

In the following computations, the working fluid is the heavy perfluorocarbon PP10. The material-dependent quantities required by the thermodynamic models include the boiling temperature, the molecular weight, the acentric factor, and the dipole moment of the molecule. Most of the required data for PP10 have been taken from Cramer (1989*a*). The acentric factor was calculated by its definition formula (see Reid, Prausnitz & Poling 1987), as a function of vapour-pressure data and critical properties. The dipole moment was taken as equal to zero, since perfluorocarbons are essentially non-polar substances.

3. Flow solver

The governing equations are discretized using a cell-centred finite-volume scheme of third-order accuracy, extended to the computation of flows with an arbitrary equation of state (Cinnella & Congedo 2005*b*). The scheme is constructed by correcting the dispersive error term of the second-order-accurate Jameson's scheme (Jameson, Schmidt & Turkel 1981). The use of a scalar dissipation term simplifies the scheme implementation with highly complex equations of state and greatly reduces computational costs. In order to preserve the high accuracy of the scheme on non-Cartesian grids, the numerical fluxes are evaluated using suitably weighted discretization formula, which take into account mesh deformations: this ensures a truly third-order accuracy on moderately deformed meshes and at least second-order accuracy on highly distorted meshes (see Rezgui, Cinnella & Lerat 2001 for details). The governing equations are integrated in time using a four-stage Runge–Kutta scheme. Local time-stepping, implicit residual smoothing and multigrid are used to drive the solution efficiently to the steady state.

The numerical method has been successfully validated for a variety of perfect and real gas flows (see Cinnella & Congedo 2005*a*, *b* and references therein). Hereinafter an example of its grid-convergence properties is provided for one of the most difficult transonic turbulent BZT flows discussed in the following. Specifically, PP10 flowing over a NACA0012 airfoil at $M_\infty = 0.85$, $\alpha = 1^\circ$, $Re = 9 \times 10^6$ and thermodynamic free-stream conditions $p_\infty/p_c = 1.08$, $\rho_\infty/\rho_c = 0.882$ is considered. The flow is characterized by compression shock waves at both airfoil surfaces and post-shock separation at the upper side. Figure 3 displays Mach number contours and wall distributions of the temperature, pressure coefficient and skin friction obtained on C-grids composed by 256×64 and 256×128 cells, respectively. The finer grid is generated from the coarser one by doubling the number of grid points in the direction normal to the wall. The outer boundary is located about 20 chords away from the airfoil. The average height of the cells closest to the wall in terms of the viscous layer coordinate is $y^+ \approx 5$ on the coarsest grid and $y^+ \approx 1$ on the finer one. Recall that $y^+ := y\sqrt{\rho_w \tau_w/\mu_w^2}$ where τ is the shear stress and the subscript w refers to wall quantities. Results obtained

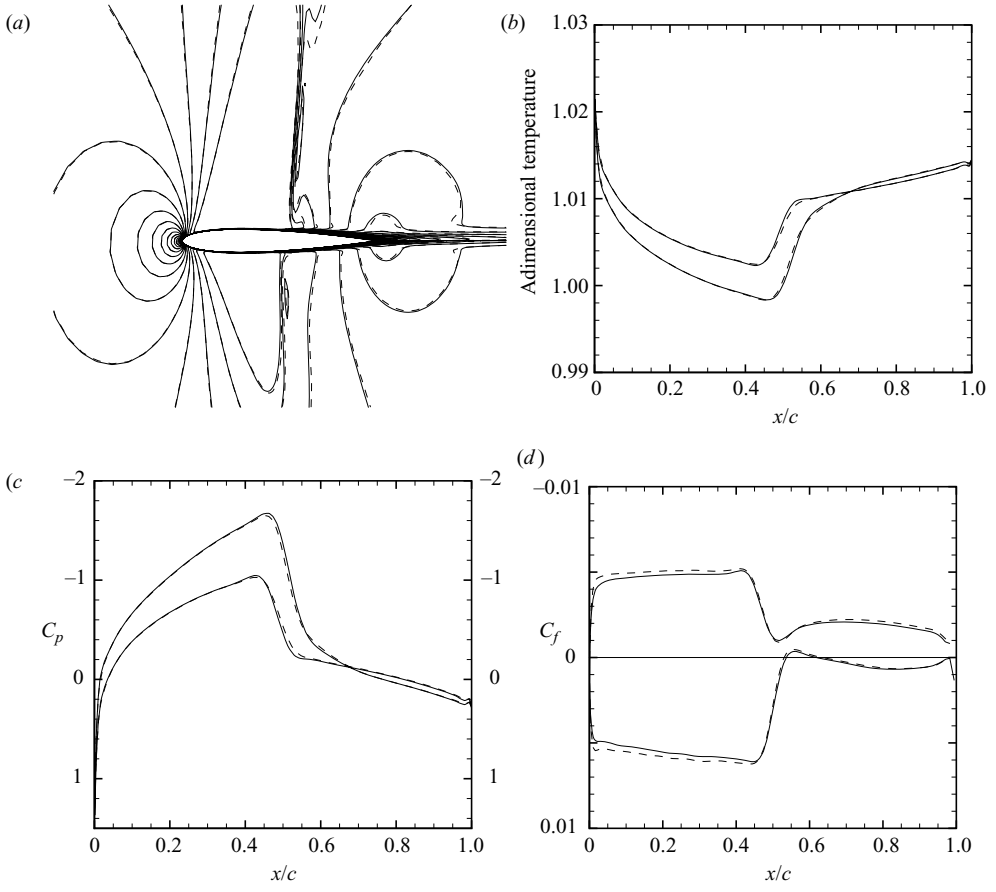

FIGURE 3. Analysis of grid convergence for the numerical method. (*a*) Iso-Mach contours, (*b*) wall temperature, (*c*) pressure coefficient, (*c*) skin friction. —, 256×128; - - -, 256×64.

on both grids are close to each other (differences within 1 % for the wall quantities), showing that the numerical solution is grid-converged.

4. Dense gas aerodynamics

The preceding numerical method is used to investigate inviscid and viscous transonic flows of a BZT dense gas (DG) past a NACA0012 airfoil. The objective is to explore the influence of dense-gas effects on the airfoil aerodynamic performance, also in comparison with reference results for a perfect gas (PFG) flowing at the same free-stream conditions.

4.1. *Choice of the operating conditions*

For a dense gas, the parameters governing the flow are, in addition to the free-stream Mach number and angle of attack, the free-stream thermodynamic conditions, i.e. the thermodynamic operation point. Since typical ORC turbine blades work in the high-subsonic/low-supersonic regimes, flows past the NACA0012 airfoil are investigated for three different free-stream conditions: high-subsonic; sonic; and low-supersonic. The angle of attack is taken fixed and equal to 1°. As mentioned in § 1, BZT inviscid steady flows with weak shocks can be considered as isentropic

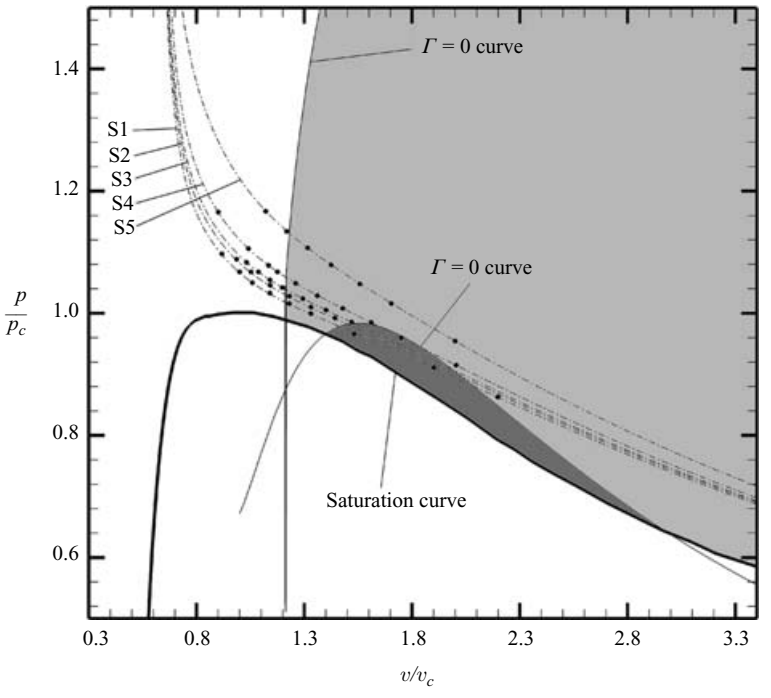

FIGURE 4. Location of the operation points (black dots) in the $p - v$ diagram.

to a first approximation. Consequently, in the (p, v)-plane, the locus of all possible thermodynamic states in the flow field lies roughly on the isentrope corresponding to free-stream conditions. The locus is approximately superposed with the arch of the isentrope included between the minimum and maximum pressures in the flow. If the locus crosses the inversion zone, the flow field exhibits a region of BZT effects. The operation points chosen for the present study are picked on five different isentropes of the (p, v)-plane. These correspond to values of the non-dimensional free-stream entropy (defined as $(s_\infty - s_c)/(R\,Z_c)$, with R the gas constant and $Z_c = p_c/(R\rho_c T_c)$ the critical compressibility factor) equal to 15.06, 15.33, 15.51 and 15.94, respectively. Figure 4 shows the five isentropes, the operation points, the inversion zone and the dense gas region ($\Gamma < 1$) for PP10. When moving from right to left along an isentrope, the free-stream fundamental derivative Γ_∞, initially positive, decreases, changes its sign where the isentrope crosses the inversion zone, reaches a minimum, and increases again (see figure 5). For high-pressure operation points, Γ_∞ is greater than one. For these points, asymptotic theories based on the assumption $|\Gamma| \ll 1$ are no longer valid. Isentropes S1 to S3 cross the inversion zone. Isentrope S4 is approximately tangent to the transition line and represents a limiting case. Finally, isentrope S5 lies completely outside the inversion zone, but crosses the extended thermodynamic region where $\Gamma < 1$. For flows with free-stream entropy S5, BZT effects cannot appear, but significant DG effects related to reverse sound speed behaviour are expected.

4.2. *Inviscid flow behaviour*

Inviscid flow computations are performed using three C-grids, formed by 136×20, 272×40 and 544×80 cells, respectively. The finest and the coarsest grids are generated by doubling or halving, respectively, the number of cells of the medium one in each direction. The outer boundary is about 20 chords away from the airfoil, and the mean

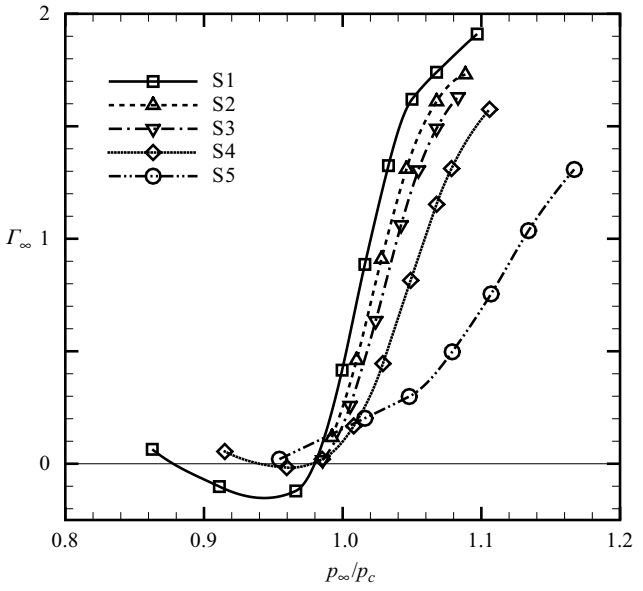

FIGURE 5. Fundamental derivative versus pressure along selected isentropes.

height of the first cell closest to the wall is about 5×10^{-2} chords on the medium grid. For most of the computations presented in the following, grid convergence for the wall pressure and Mach number distributions has been obtained on the medium grid. However, the results presented in the following have been obtained on the finest grid. For a more accurate evaluation of the solution's convergence, the scheme's order of convergence is estimated following Roache's method (Roache 1998), based on Richardson extrapolation. Given three numerical solutions computed on grids of increasing spacing, with constant grid refinement ratio r, the actual order of convergence is:

$$q = \ln\left(\frac{f_3 - f_2}{f_2 - f_1}\right) \Big/ \ln(r),$$

where f is a solution functional and indices 1 and 3 refer to the finest and the coarsest grid solution, respectively. For the present computations, a computed order of convergence of 2.2 or higher is found, based on the lift coefficient C_l. This value is used to compute Roache's grid convergence index (GCI) on the finest and medium grid, which represents an estimate of how far the numerical solution is from its asymptotic value. GCIs of 0.08 % and 0.39 % are found for the finer and the medium grid, respectively, indicating that the solution is well within the asymptotic range. Such values are likely to be conservative.

4.2.1. *Dense gas flows in high-subsonic free stream*

The reference solution for a perfect diatomic gas (specific heat ratio $\gamma = 1.4$) flowing at $M_\infty = 0.85$, $\alpha = 1^\circ$ is first considered. This is a well-known test case, which has been often used for the validation of numerical schemes for the Euler equations (see for instance Dervieux, van Leer & Rizzi 1989; Cinnella & Congedo 2005*b*): therefore, detailed results are not reported for brevity. The flow is characterized by two shocks at about 85 % of the chord at the suction side, and 63 % at the pressure side. The

computed lift and drag coefficients, and lift-to-drag ratio are:

$$C_l = 0.373, \quad C_d = 5.74 \times 10^{-2}, \quad C_l/C_d = 6.51.$$

These values agree reasonably with other results reported for the same case (Dervieux *et al.* 1989). Then, flows of the dense gas PP10 past the same airfoil are computed. Results for lift, drag and lift-to-drag ratio obtained for different choices of the free-stream fundamental derivative and free-stream entropy are summarized in figure 6, along with some results from small-disturbance theory, discussed later in this section. For the lowest values of Γ_∞, the drag is almost equal to zero (order 10^{-4}), and increases monotonically with it. The lift coefficient initially grows, reaches a maximum, and then drops dramatically. The lift-to-drag ratio is poor for high Γ_∞ flows, but tends to infinity as the free-stream value of the fundamental derivative approaches unity. The best aerodynamic performance, offering a satisfactory trade-off between high lift and low drag is obtained for Γ_∞ approximately in the range 1–1.3; in such conditions, the flow displays higher lift and significantly reduced wave drag compared to PFG results. Note that the curves exhibit sudden changes in slope, related to corresponding changes in the flow patterns. In order to explain the computed behaviour of the aerodynamic performance, a detailed analysis of the flow fields obtained for each operating condition is undertaken, which allows us to identify three typical flow regimes, described in the following.

For flows characterized by relatively low free-stream pressures and small values of the free-stream fundamental derivative (Γ_∞ less than about 1), the computed lift-to-drag ratio is extremely high, although the lift coefficient is lower than in the perfect gas case. Inspection of the Mach number field shows that such flows remain entirely subsonic. Since the free stream is uniform and steady and no viscous effects are taken into account, the flow should also be isentropic, with drag coefficient exactly equal to zero. In practice, small entropy gradients are generated close to the wall, because of numerical errors introduced by the numerical scheme and boundary conditions, which lead to small non-zero values, $O(10^{-4})$, for the computed drag. As a consequence, the computed lift-to-drag ratio is not unbounded, but $O(10^3)$. An estimate for the critical Mach number, M_c, in BZT transonic flows with $\Gamma_\infty \approx 0$, $\Lambda_\infty \approx 0$, has been provided by Cramer & Tarkenton (1992), using an extended transonic small-disturbance theory. These authors demonstrated that for flows with $\Lambda_\infty < 0$, at least one sonic point necessarily appears in the flow field. On the contrary, for flows characterized by $\Lambda_\infty > 0$, i.e. at the high-pressure border of the inversion zone, sonic points appear if the free-stream Mach number is greater than the critical value:

$$M_c = \left(1 - \frac{\Gamma_\infty^2}{\Lambda_\infty}\right)^{-1/2} \approx 1 - \frac{\Gamma_\infty^2}{2\Lambda_\infty}, \tag{4.1}$$

where Λ is the previously defined second nonlinearity parameter, representing the rate of change of Γ along an isentrope. Figure 7(*a*) shows the distribution of Λ_∞ associated to the chosen operation points (Λ_∞ is evaluated numerically using second-order weighted central differences). Figure 7(*b*) displays the critical Mach numbers predicted by formula (4.1) versus the maximum Mach number in the computed flow field for flow cases with $\Lambda_\infty > 0$. Since the free-stream Mach number is always equal to 0.85, then for operating conditions such that $M_c < M_\infty$, the flow is expected to be supercritical according to the small-disturbance theory, i.e. the point of coordinates (M_c, M_{max}) should lie within quadrant *II* of figure 7(*b*) ($M_{max} > 1$). On the contrary, for operating conditions such that $M_c > M_\infty$, the same point should lie in quadrant

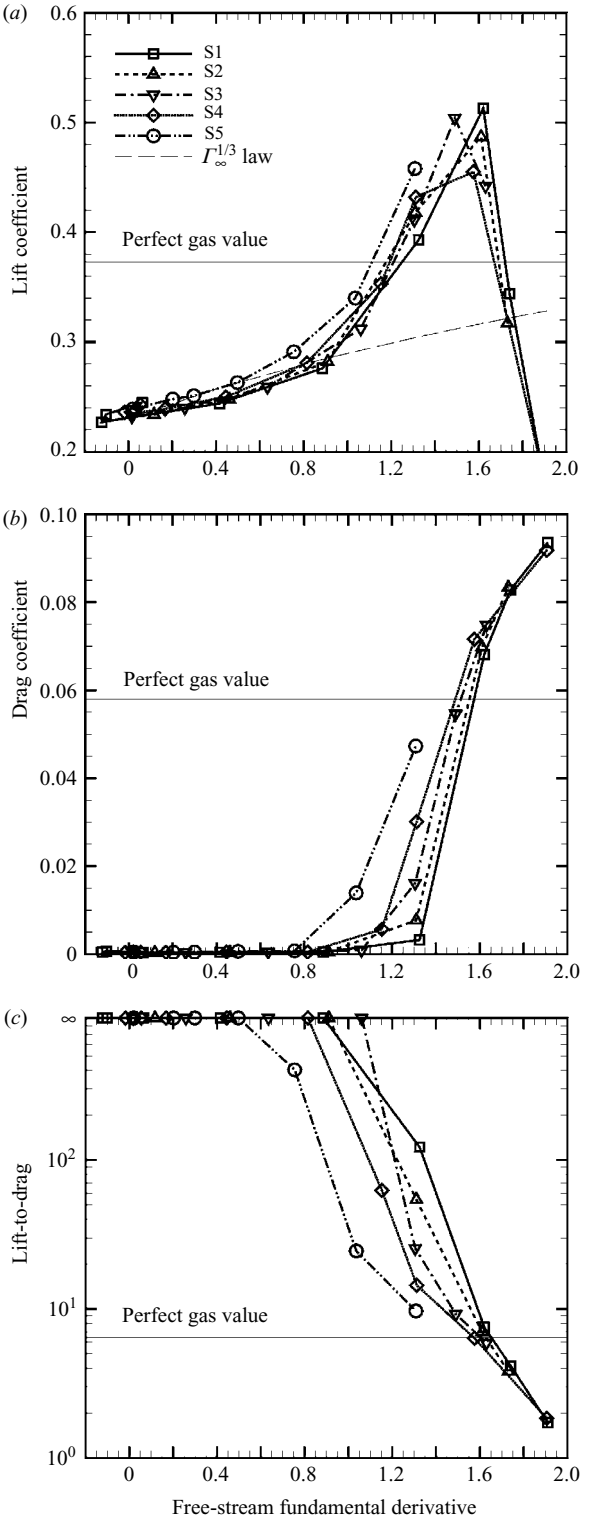

FIGURE 6. Aerodynamic coefficients versus free-stream fundamental derivative for flow at $M_\infty = 0.85$, $\alpha = 1^\circ$ past a NACA0012. In (*a*) results from the small-disturbance theory for near sonic flows with small Γ_∞ are also reported ($\Gamma_\infty^{1/3}$ law).

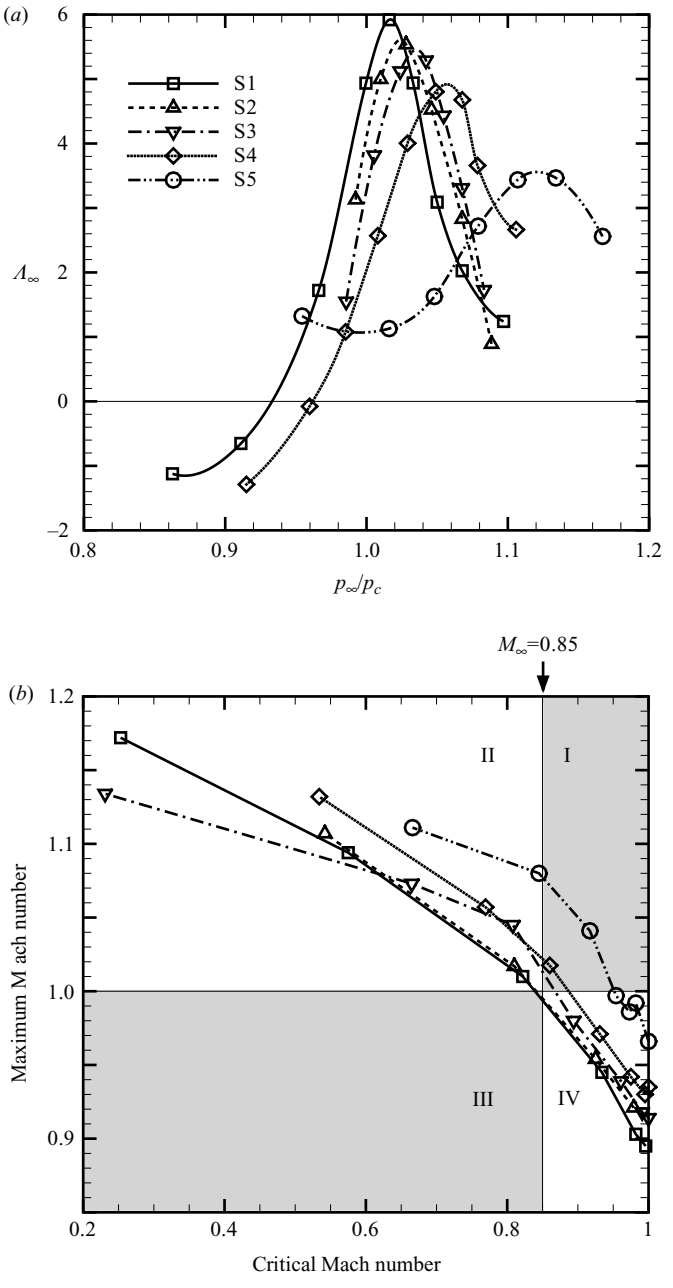

FIGURE 7. Second nonlinearity parameter (*a*) and estimated critical Mach number versus maximum flow Mach number (*b*) for DG flows past the NACA0012 airfoil at $M_\infty = 0.85$, $\alpha = 1^\circ$ at different free-stream thermodynamic conditions.

IV ($M_{max} < 1$). For points lying in shaded regions, predictions from small-disturbance theory are not verified. Inspection of figure 7(*b*) shows that there is good agreement between estimate (4.1) and the present numerical results. The estimate just fails for operating conditions $p_\infty/p_c = 1.07$, $\rho_\infty/\rho_c = 0.850$ ($\Gamma_\infty = 1.15$), where the flow is found to be supercritical although M_∞ is slightly below M_c, and for conditions

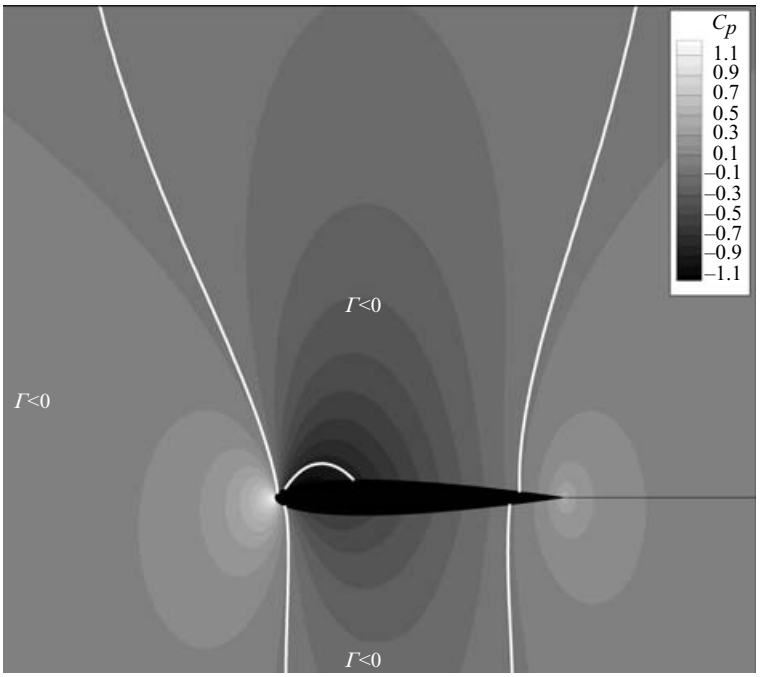

FIGURE 8. Pressure coefficient contours and $\Gamma = 0$ contours for operating conditions $p_\infty/p_c = 0.986$, $\rho_\infty/\rho_c = 0.658$, $\Gamma_\infty = 0.017$ (BZT subcritical regime).

$p_\infty/p_c = 0.821$, $\rho_\infty/\rho = 0.821$ ($\Gamma_\infty = 0.335$), where supercritical flow is also found in spite of free-stream conditions below the critical value. In the first case, the estimated critical Mach number (equal to 0.858), is very close to the free-stream value, and the disagreement may be due to numerical inaccuracies in the evaluation of Λ. On the other hand, the operation point corresponding to the latter condition lies quite far outside the inversion zone, and the use of approximation (4.1) is not really justified.

Subcritical (shock-free) flow can be obtained even for operating conditions outside the inversion zone. This leads us to conclude that beneficial effects on the aerodynamic performance can also be obtained using non-BZT working fluids, provided they display a sufficiently large region of very small, albeit positive, Γ values. A typical pressure contour plot for subcritical flow cases is displayed in figure 8 along with $\Gamma = 0$ contours. Typical distributions of the Mach number, pressure coefficient, fundamental derivative, and sound speed at the wall are presented in figure 9. When a fluid particle from the free stream approaches the airfoil along the wall streamline, it undergoes a compression and the local fundamental derivative grows, reaching a maximum at the stagnation point where $\Gamma_{max} \approx 1.5$–2. Then, Γ suddenly drops when the flow begins to expand accelerating over the top of the airfoil. Both pressure coefficient and Γ variations in the neighbourhood of the stagnation point are very large: if Γ_∞ is sufficiently small, roughly $\Gamma_\infty < 1$, the local fundamental derivative becomes smaller than 1, or even negative, less than 0.01 chords downstream of the leading edge: consequently, the speed of sound grows sharply enough to couterbalance the increase of velocity and the flow remains subsonic. The smaller Γ, the steeper is the sound speed growth. As high values of the sound speed are associated to low values of the adiabatic compressibility coefficient $\beta_s = (1/\rho)(\partial\rho/\partial p)_s = 1/(\rho a^2)$, flows with low Γ_∞ conserve a behaviour closer to the incompressible one. This can be seen better by using

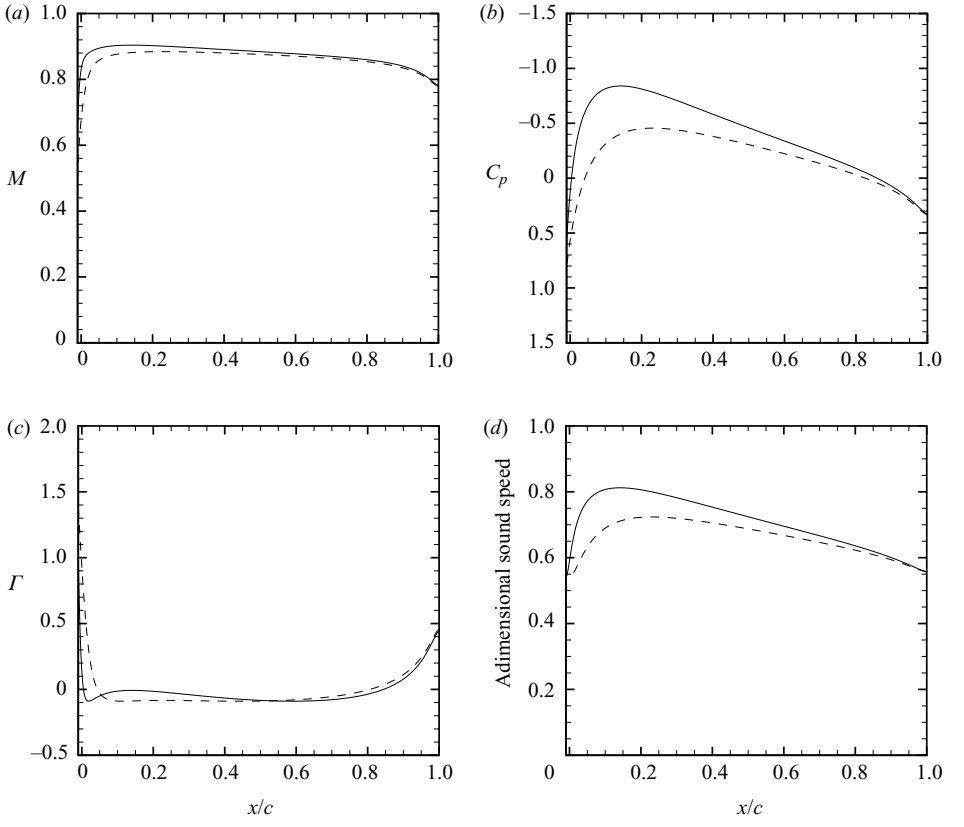

FIGURE 9. Wall distributions of the Mach number, pressure coefficient, fundamental derivative and sound speed for operating conditions $p_\infty/p_c = 0.986$, $\rho_\infty/\rho_c = 0.658$, $\Gamma_\infty = 0.017$ (BZT subcritical regime). —, upper surface; - - -, lower surface.

results from the small transonic disturbance theory (Cramer & Tarkenton 1992). In fact, writing the classical transonic similarity parameter in terms of Γ_∞ (Hayes 1966):

$$K = \frac{1 - M_\infty^2}{(\Gamma_\infty \varepsilon)^{2/3}},$$

with ε the airfoil thickness, and using the well-known Prandtl–Glauert similarity law:

$$C_p = \frac{C_p^{inc}}{\varepsilon K^{1/2}},$$

where C_p^{inc} is the pressure coefficient for the same airfoil, albeit in incompressible flow, we find that:

$$C_p = \frac{C_p^{inc} \Gamma_\infty^{1/3}}{\varepsilon^{2/3} \sqrt{1 - M_\infty^2}}, \tag{4.2}$$

that is, the pressure coefficient approximately grows as $\Gamma_\infty^{1/3}$, and a similar behaviour can be expected for the lift. For $\Gamma_\infty = 0$, equation (4.2) predicts $C_p = 0$. Of course, this does not occur in practice, because of higher-order effects in the airfoil nose region (for an estimate of the pressure coefficient variation for flows with $\Gamma_\infty = 0$, $\Lambda_\infty = 0$ around airfoils with a parabolic nose, see Rusak & Wang 1997). Results plotted in figure 6(*a*)

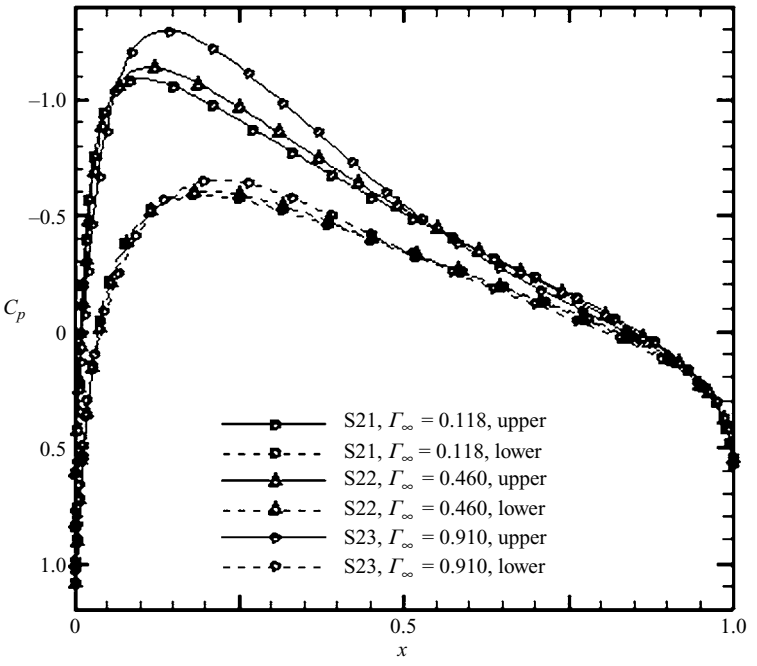

FIGURE 10. Wall distributions of the pressure coefficient for different operating conditions in the BZT subcritical regime.

show how, for flow conditions characterized by low Γ_∞, the lift coefficient actually follows quite well a law of the form $C_l = C_{l_0}(1 + \Gamma_\infty)^{1/3}$, where the coefficient C_{l_0} has been computed from numerical results obtained for $\Gamma_\infty \approx 0$. In practice, however, owing to nonlinear effects and strong gradients in the leading-edge region, subcritical flow is also obtained for free-stream conditions characterized by values of Γ_∞ not really 'small', but $O(1)$. In this sense, predictions from the small-disturbance theory are conservative. Pressure coefficient distributions for different values of Γ_∞ (at fixed entropy) are shown for completeness in figure 10, which illustrates well the growth of C_p with Γ_∞.

In summary, for 'sufficiently low' Γ_∞ (<1):

(*a*) the flow past the airfoil is subcritical;

(*b*) the drag coefficient vanishes;

(*c*) lift is lower than in the perfect gas case, because of the reduced flow compressibility;

(*d*) lift tends to increase with Γ_∞.

When Γ_∞ is approximately in the range 1–1.5, the flow patterns change dramatically. In this range, a significant growth in both lift and drag is observed with respect to the previous case (see figure 6*a*). Nevertheless, the lift-to-drag ratio is still about one order of magnitude greater than in the perfect gas case owing, on the one hand, to high values obtained for the lift and, on the other, to very low wave drag. In this regime, the flow becomes supercritical, in agreement with estimate (4.1). For operating conditions lying on S1 to S4, the flow-field displays significant BZT effects, which are responsible for the high aerodynamic performance. On the other hand, no BZT effects appear for operating conditions S5; however, since the fundamental derivative takes very small albeit positive values, the overall flow behaviour does not differ very much from the other two cases: the flow patterns are similar to those obtained at

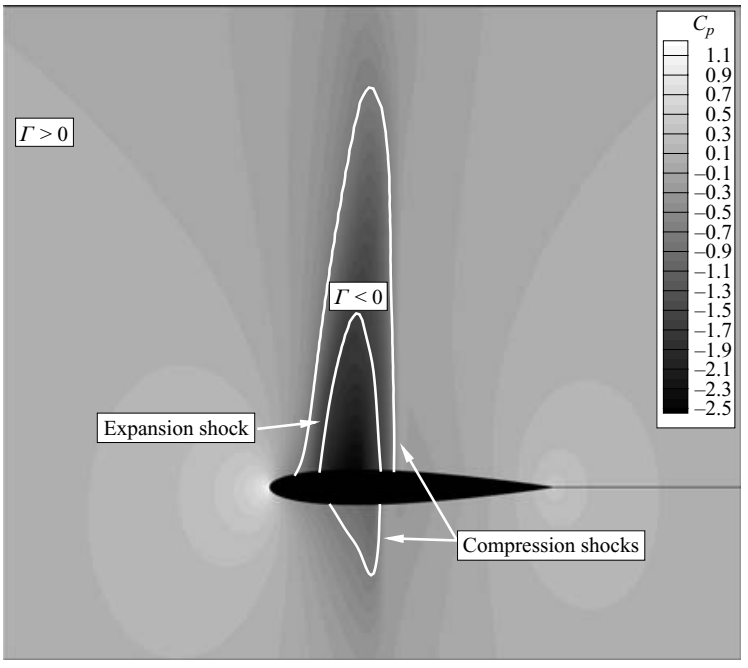

FIGURE 11. Pressure coefficient contours and $\Gamma = 0$ contours for operating conditions $p_\infty/p_c = 1.05$, $\rho_\infty/\rho_c = 0.877$, $\Gamma_\infty = 1.31$ (low-pressure transonic BZT regime).

operating conditions S1–S4 at slightly higher pressures. A typical view of the pressure contours for this flow regime is presented in figure 11, whereas figure 12 shows the wall distributions of the Mach number, pressure coefficient, fundamental derivative, and sound speed. For this kind of flow, characterized by higher free-stream Γ, the reversed behaviour of the sound speed associated to flow regions with $\Gamma < 1$ is delayed, and the flow expands to supersonic conditions downstream of the leading edge. Along the upper surface, if the free-stream values of Γ and of the entropy are sufficiently low, Γ may become negative just downstream of the stagnation point, where the pressure is still falling steeply, so that an expansion shock is generated a short distance from the airfoil wall. Downstream of this shock, the pressure coefficient drops to values much lower than in the perfect gas case. The expansion shock is followed first by a continuous expansion and then by a gradual compression, which terminates in a compression shock as soon as the flow exits the inversion zone. Increasing Γ_∞ and/or the free-stream entropy, the change of sign of the fundamental derivative is delayed, or never happens (this is the case of conditions S5), and no expansion shock appears, the flow being always recompressed through a classical shock at the rear part of the upper surface. Along the lower surface, only a weak compression shock forms. Both expansion and compression shocks have jump conditions in the vicinity of the transition line: the entropy jump across such shocks (normalized with the free-stream entropy) is $O((\Delta p)^4)$, whereas it is $O((\Delta p)^3)$ for perfect gas flow. Accordingly, the wave drag is approximately one order of magnitude lower with respect to the PFG value. In summary, flows in the second regime (called hereinafter the low-pressure transonic BZT regime) are supercritical and characterized by high lift and very low wave drag, because shock waves occurring in the vicinity of the transition line are much weaker than usual. For operating conditions characterized by sufficiently low values of Γ_∞

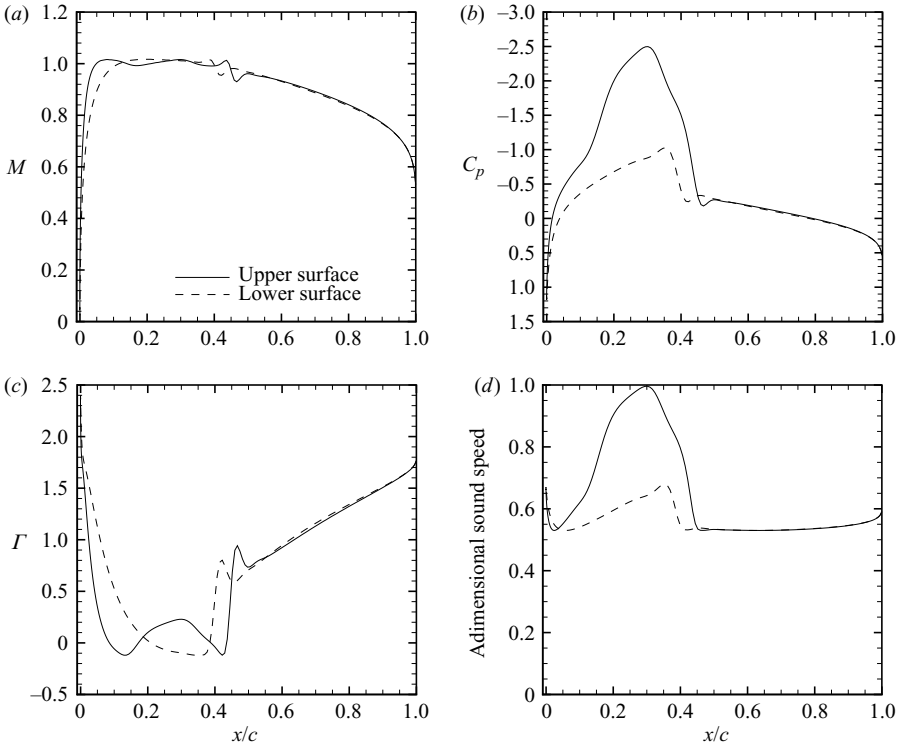

FIGURE 12. Wall distributions of the Mach number, pressure coefficient, fundamental derivative and sound speed for operating conditions $p_\infty/p_c = 1.05$, $\rho_\infty/\rho_c = 0.877$, $\Gamma_\infty = 1.31$ (low-pressure transonic BZT regime). —, upper surface; - - -, lower surface.

and s_∞, the aerodynamic performance is even further improved by the formation of an expansion shock close to the leading edge, which strongly enhances the suction peak, and consequently the lift, at the airfoil upper surface. This mechanism is similar to that observed by Cinnella & Congedo (2005*a*) for BZT flows of a van der Waals gas.

When Γ_∞ is even higher, the flow becomes qualitatively similar to that of a perfect gas since the region of flow characterized by $\Gamma < 0$ becomes smaller and finally disappears. In this third regime (which will be called the high-pressure transonic BZT regime), the lift coefficient drops abruptly and the drag increases, owing to stronger entropy gradients generated across the shocks. Consequently, the lift-to-drag ratio becomes very poor. Typical pressure contours for this kind of flow are shown in figure 13.

4.2.2. *Near-sonic and low-supersonic free stream*

Since ORC turbomachinery frequently works in the high-transonic or low-supersonic regime, dense flows at $M_\infty = 0.9999$ and $M_\infty = 1.1$ ($\alpha = 1^\circ$) past the NACA0012 airfoil are also investigated. Only isentropes S1, S4 and S5 are retained for this study.

The reference solution (not shown for brevity) for a diatomic perfect gas flow at $M_\infty = 0.9999$ and $\alpha = 1^\circ$ is characterized by strong shocks attached to the airfoil trailing edge and displays a very poor aerodynamic performance:

$$C_l = 8.98 \times 10^{-2}, \quad C_d = 1.06 \times 10^{-1}, \quad C_l/C_d = 8.47 \times 10^{-1}.$$

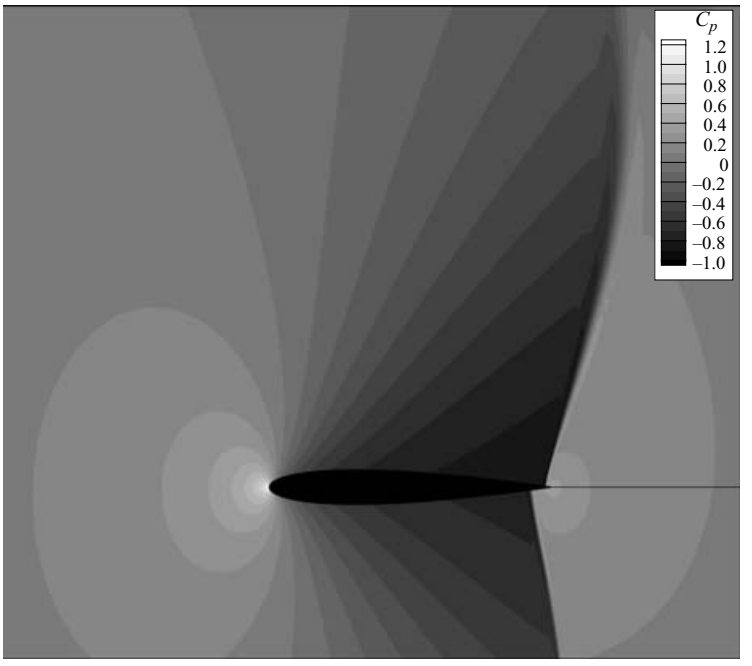

FIGURE 13. Pressure coefficient contours and $\Gamma = 0$ contours for operating conditions $p_\infty/p_c = 1.17$, $\rho_\infty/\rho_c = 1.11$, $\Gamma_\infty = 1.91$ (high-pressure transonic BZT regime).

A similarly poor performance is obtained at $M_\infty = 1.1$, owing to the formation of a bow-shock upstream of the airfoil nose and oblique shocks attached to the trailing edge. In this case, the computed lift and drag coefficients, and their ratio, are:

$$C_l = 9.11 \times 10^{-2}, \quad C_d = 1.06 \times 10^{-1}, \quad C_l/C_d = 8.63 \times 10^{-1}.$$

Dense gas flows at $M_\infty = 0.9999$ are always beyond critical conditions: very different flow patterns are found according to the operation point considered. The more complex patterns are obtained for conditions S1, where non-classical structures owing to BZT effects appear. Conversely, only classical behaviours are found for flow conditions S5, and the flow is qualitatively similar to that of a perfect gas with the same free-stream conditions. An intermediate behaviour is displayed by flows at conditions S4.

Flow patterns at $M_\infty = 1.1$ are much simpler and do not change much with operating conditions: they are always characterized by a bow-shock, even for negative free-stream Γ, since the strong compression upstream of the stagnation point quickly drives the thermodynamic state outside the (small) inversion zone; in addition, compressive waves form at the trailing edge. These can be either classical oblique shocks, or mixed compression waves. Mixed waves are associated with operating conditions with low Γ_∞, and progressively change into oblique shocks when this parameter increases.

Plots of the lift and drag coefficients and their ratio versus free-stream fundamental derivatives for flows with sonic free stream are shown in figure 14. Markedly different curves are obtained for different free-stream entropies, owing to dramatic changes in the flow patterns. Similarly to the preceding transonic case, the lift coefficient displays an optimum for $\Gamma_\infty = O(1)$. For Γ_∞ less than approximately 0.8–1, the lift coefficient is twice, or more, the PFG value. On the other hand, since the flow is supercritical

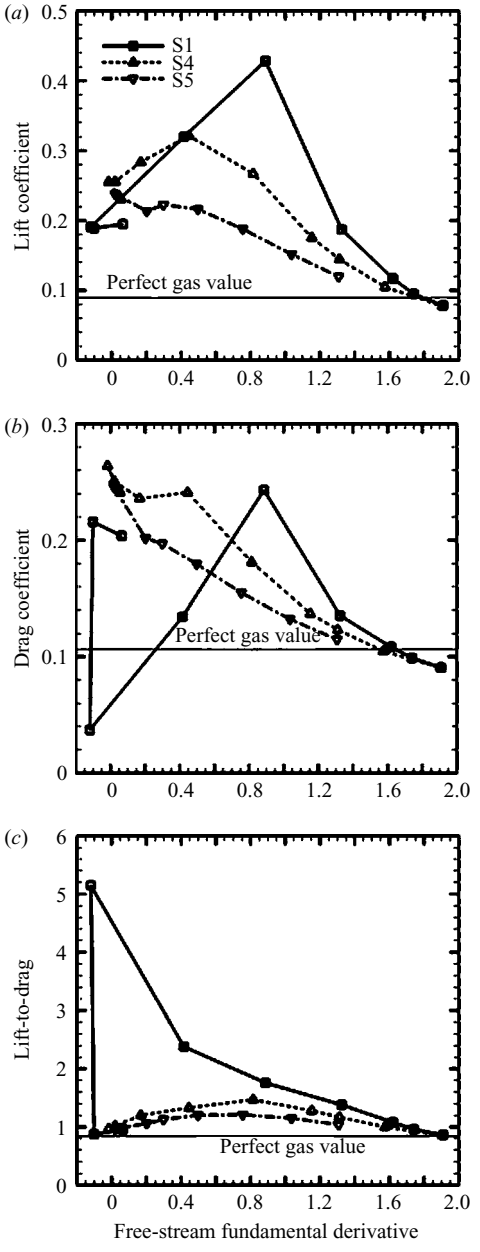

FIGURE 14. Aerodynamic coefficients versus free-stream fundamental derivative for flows at $M_\infty = 0.9999$, $\alpha = 1^\circ$ past a NACA0012.

at all operating conditions, the drag coefficient remains approximately of the same order of magnitude as in PFG flow, owing to the appearance of strong discontinuities. As a consequence, efficiency improvements due to the use of a BZT working fluid are not as impressive as in the previous transonic case; nevertheless, the lift-to-drag ratio is above the PFG value for the whole range of operating conditions considered in the study, and it is more than five times greater at peak performance conditions. At operating conditions $p_\infty/p_c = 0.863$, $\rho_c = 0.455$ ($\Gamma_\infty = 0.064$) and $p_\infty/p_c = 0.911$,

$\rho_c = 0.526$ ($\Gamma_\infty = -0.101$) (isentrope S1), the drag coefficient is specially large, owing to the occurrence of weak bow-shocks upstream of the airfoil nose in spite of subsonic free-stream conditions (see for example the pressure coefficient and $\Gamma = 0$ contour plot for the latter operation point on figure 15*a*). This non-classical effect, related to the non-monotonic variation of the Mach number with pressure in dense gases, has been described by Cramer & Tarkenton (1992) for flows of the fluorocarbon PP11 over a circular arc airfoil, and by Wang & Rusak (1999) and Cinnella & Congedo (2005*a*) for flows of van der Waals gases over a NACA0012 airfoil, and will not be discussed further. At peak efficiency operating conditions $p_\infty/p_c = 0.966$, $\rho/\rho_c = 0.653$ ($\Gamma_\infty = -0.121$) on isentrope S1, the flow field changes radically. When the flow approaches the stagnation point, Γ grows beyond 1, the Mach number behaves in a classical way and no bow-shock is formed. The flow is characterized merely by a classical shock wave located about mid-chord at the upper surface. This shock has jump conditions in the vicinity of the transition line, and the associated losses are very low. Consequently, the drag coefficient reaches a minimum. Pressure coefficient contour plots for this case are shown in figure 15(*b*), where $\Gamma = 0$ contours are also reported. Finally, at higher operating pressures/entropies, the flow returns to similar to that of a PFG.

Figure 16 shows the lift and drag coefficients and the lift-to-drag ratio for supersonic flow cases: they increase with operating pressure for flow conditions such that $\Lambda_\infty < 0$, and reverse their behaviour when $\Lambda_\infty > 0$. The lift and lift-to-drag ratio are greater than in the reference PFG case for almost all of the investigated operation points albeit the drag exerted on the airfoil is somewhat higher. For these flow conditions, optimal aerodynamic performance is no longer obtained for $\Gamma_\infty = O(1)$, but instead for $\Gamma_\infty \approx 0$. Typical pressure coefficient contours at $M_\infty = 1.1$ are shown in figure 17.

4.3. *Viscous behaviour*

4.3.1. *Laminar flow over a flat plate*

In order to investigate the influence of DG effects on the development of a laminar boundary layer, the classical problem of laminar flow over a flat plate with no pressure gradient is first considered. The incoming flow has $M_\infty = 0.2$ and $Re = 500$, based on inlet density and velocity, and unit plate length and the plate wall is adiabatic. Results are computed in the rectangular domain $[0, 14] \times [0, 5]$ (the plate leading and trailing edges being located in $(1, 0)$ and $(13, 0)$, respectively), discretized by a Cartesian grid of 140×50 cells, stretched in the direction normal to the wall, with first-cell height about 10^{-2}. The numerical results are compared to Blasius' solution for incompressible boundary layers. Figure 18(*a*) compares skin friction distributions obtained for a perfect gas and for a dense gas at operating conditions close to the transition line ($p_\infty/p_c = 0.976$, $\rho_\infty/\rho_c = 0.571$). In both cases, numerical results agree with theory, compressibility and dense gas effects being negligible. In order to explore dense gas effects, the flow is also computed at $M_\infty = 0.9$ and $M_\infty = 2.0$. The fluid viscosity has been rescaled in order to conserve both Mach and Reynolds numbers. At $M_\infty = 0.9$, results for both operating conditions are still close to Blasius' solution, the coupling between the viscous and the thermal boundary layer remaining weak. At $M_\infty = 2$, friction heating becomes more significant, leading to a growth of boundary-layer thickness for the perfect gas, in agreement with theory and results available in the literature (see for example Schlichting & Gersten 2003); conversely, for the dense gas, the higher specific heat limits such growth (the Eckert number for DG flows under investigation is one order of magnitude lower than in PFG flows) and the velocity profile remains close to the incompressible one (figure 18*b*). This agrees reasonably

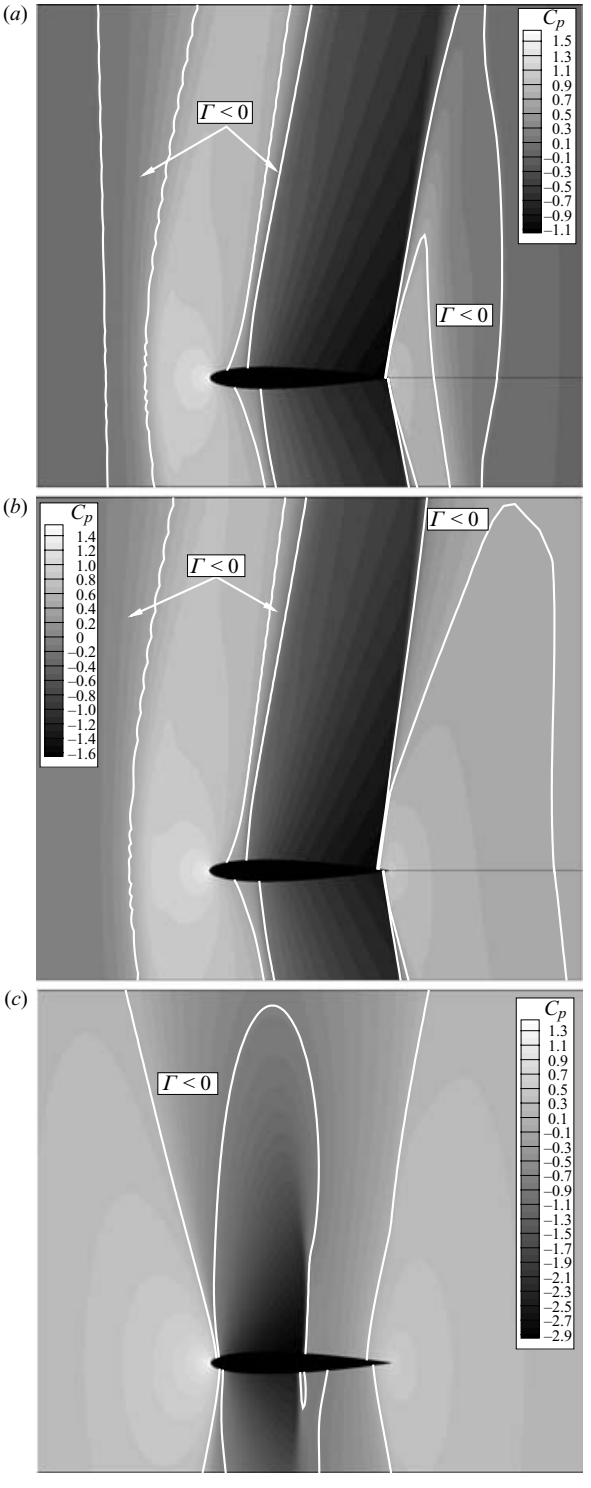

FIGURE 15. Pressure coefficient contours for flow conditions (*a*) $p_\infty/p_c = 0.863$, $\rho_\infty/\rho_c = 0.455$, $\Gamma_\infty = 0.064$, (*b*) $p_\infty/p_c = 0.911$, $\rho_\infty/\rho_c = 0.526$, $\Gamma_\infty = -0.101$, (*c*) $p_\infty/p_c = 0.966$, $\rho_\infty/\rho_c = 0.653$, $\Gamma_\infty = -0.121$. $M_\infty = 0.9999$, $\alpha = 1°$.

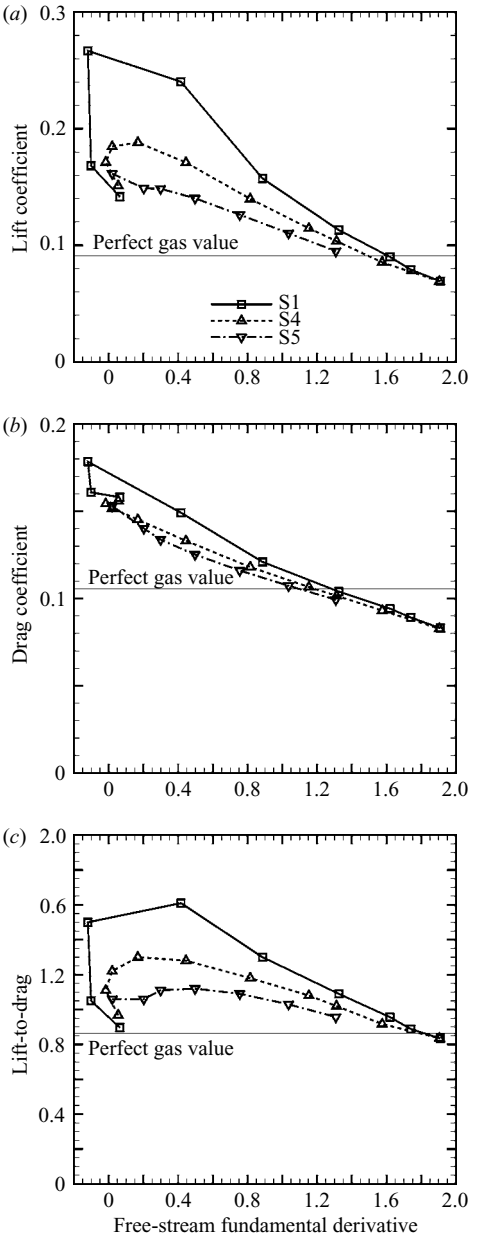

FIGURE 16. Aerodynamic coefficients versus free-stream fundamental derivative for flows at $M_\infty = 1.1$, $\alpha = 1^\circ$ past a NACA0012.

with results previously reported by Kluwick (2004) for laminar zero-pressure-gradient boundary layers of dense gases with moderately large free-stream Mach numbers.

4.3.2. *Laminar transonic flows past an airfoil*

The next series of results concerns the symmetric (zero incidence) laminar flow past the NACA0012 airfoil, at $M_\infty = 0.85$ and $Re = 1000$, Re being the Reynolds number based on the free-stream conditions and the airfoil chord. The airfoil wall is adiabatic. Computations are performed using a half-C grid made by 134×68 cells, with the

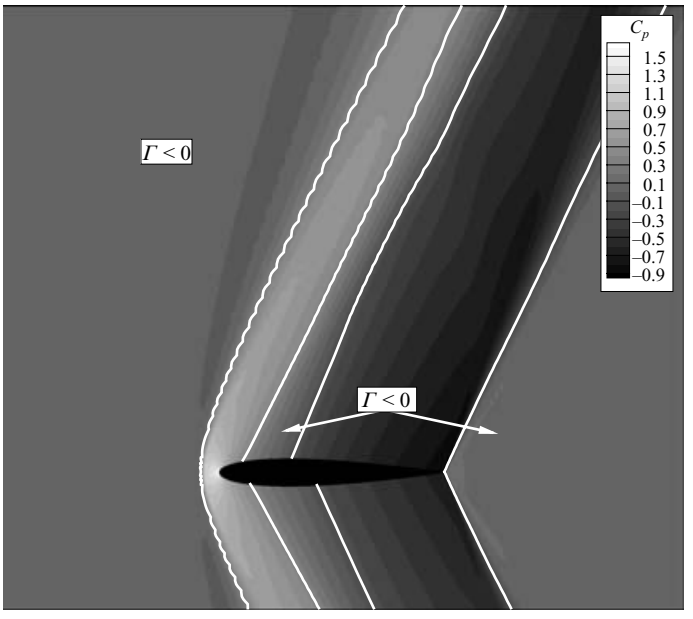

FIGURE 17. Pressure coefficient contours for flow conditions $p_\infty/p_c = 0.911$, $\rho_\infty/\rho_c = 0.526$, $\Gamma_\infty = -0.101$, $M_\infty = 1.1$, $\alpha = 1°$.

mean height of the first cell closest to the wall equal to about 0.0001 chords, and outer boundary located approximately 20 chords away from the airfoil. Computations performed on a finer grid of 268×136 cells show that the GCI based on the drag coefficient is less than 3 %.

Mach number contours for the flow of a perfect gas are depicted in figure 19(*a*): the flow over-expands to supersonic conditions, then recompresses through a shock wave approximately 0.8 chords downstream of the leading edge; the boundary layer separates at about 95 % of the chord. The computed drag coefficient is equal to 0.1848.

Let us compare this solution with that obtained for PP10 flowing at the same conditions of Mach and Reynolds number and free-stream thermodynamic conditions $p_\infty/p_c = 1.01$, $\rho_\infty/\rho_c = 0.676$, $\Gamma_\infty = 0.168$. With the preceding choice of operating conditions, the flow is subcritical. Except in the stagnation-point region, Mach-number variations through the flow are very small and the Mach number remains less than one and close to the free-stream value almost everywhere in the flow (see Mach contours in figure 19*b*).

Figure 20 shows the pressure and the skin friction coefficients at the wall for the two cases. The dense gas flow remains attached. When the flow expands from stagnation conditions, the boundary layer begins to develop. For a perfect gas, the flow accelerates to supersonic conditions, which promotes boundary-layer growth. On the contrary, for the dense gas, the flow remains subsonic during the whole expansion; moreover, the boundary layer is subject to a much stronger favourable pressure gradient. As a consequence, boundary-layer growth is slower. Accordingly, the skin friction coefficient in the leading-edge region takes higher values for the dense gas with respect to the perfect gas. When the flow begins to recompress, skin friction drops in both cases. Nevertheless, it remains slightly higher for the dense gas, and no

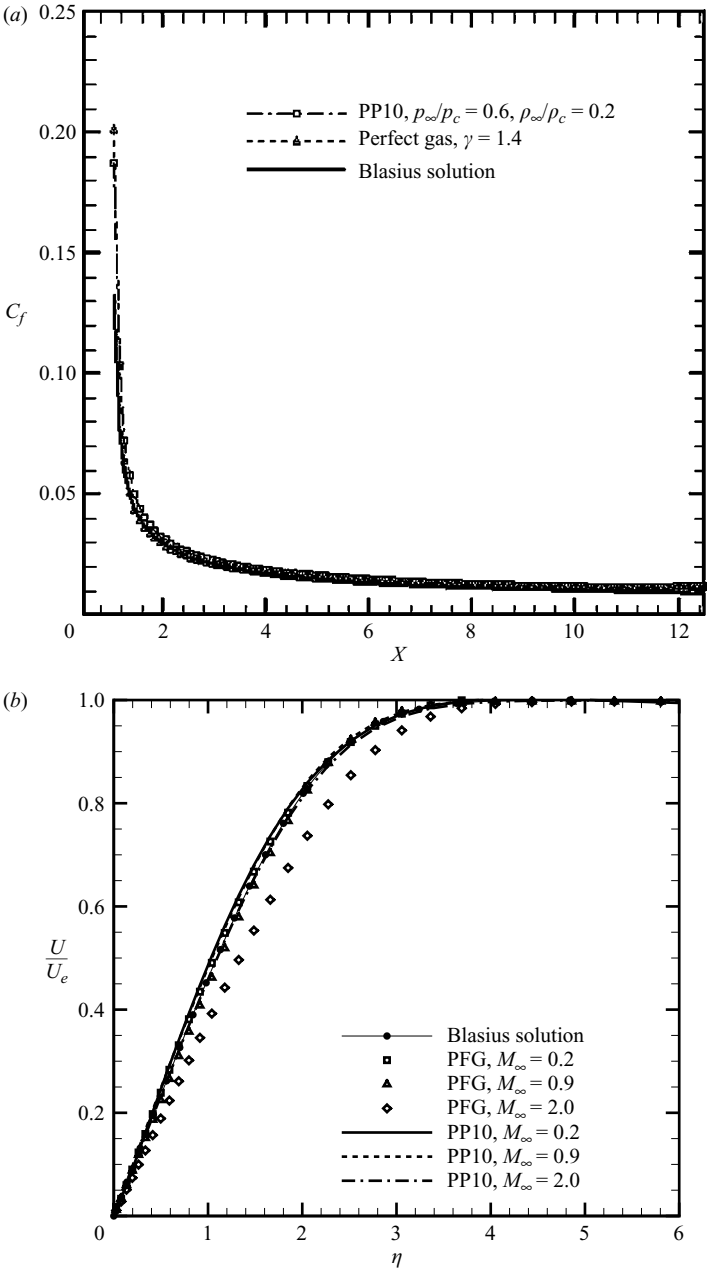

FIGURE 18. Laminar flow over a flat plate ($Re = 500$). (*a*) Skin friction distributions for perfect and dense gas flows at $M_\infty = 0.2$. (*b*) Velocity profiles at different Mach numbers.

separation point appears. The computed drag coefficient for DG flow, $C_d = 0.1652$, is about 10 % lower than the PFG value.

A supersonic flow ($M_\infty = 2$, $Re = 1000$) over the same airfoil is also considered. In this case, a bow shock forms ahead of the airfoil nose in both perfect and dense gas flow (thermodynamic conditions $p_\infty/p_c = 1.01$, $\rho_\infty/\rho_c = 0.676$). This time, the boundary layer experiences a supersonic outer flow both for the perfect and the dense

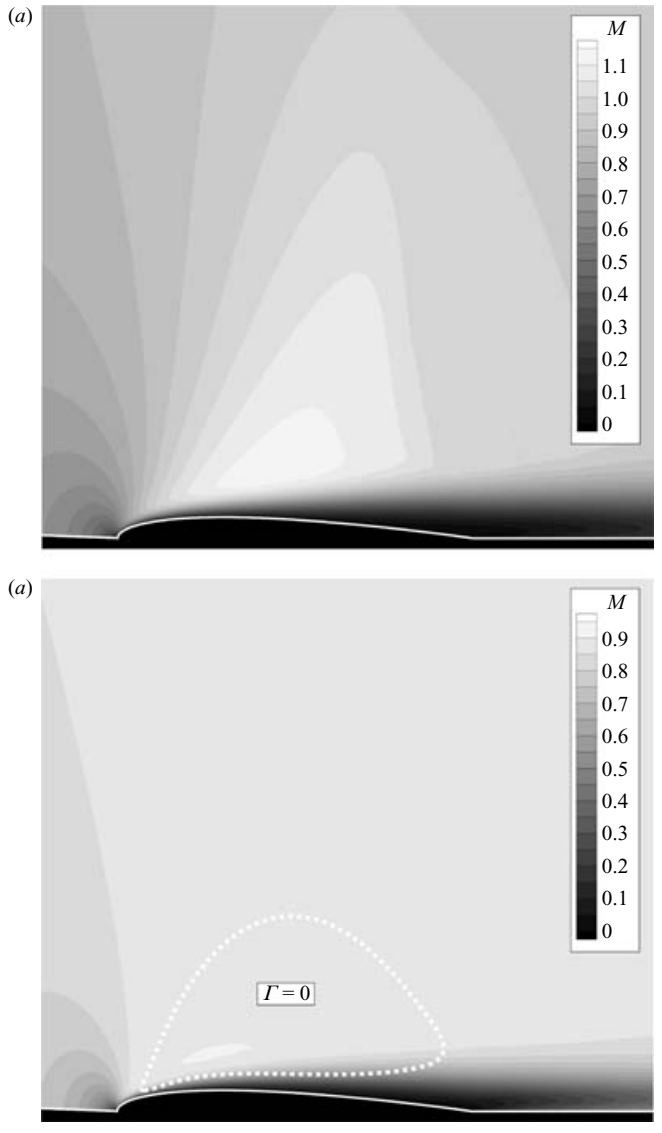

FIGURE 19. Iso-Mach contours and streamlines for laminar flow over a NACA0012 airfoil ($Re = 1000$, $M_\infty = 0.85$). (*a*) Perfect gas, (*b*) dense gas at thermodynamic conditions $p_\infty/p_c = 1.01$, $\rho_\infty/\rho_c = 0.676$.

gas case. Nevertheless, friction heating is much lower in the second case: this leads to a thinner boundary layer and to lower skin friction (see velocity profiles and skin friction distributions in figure 21*b*, *c*; the pressure coefficient is also shown for completeness). Here again, the computed drag coefficient for the dense gas, $C_d = 0.1929$, is much lower (less 16 %) with respect to the perfect gas ($C_d = 0.2309$).

4.3.3. *Turbulent flow behaviour*

The last series of results is intended to provide for the first time a data set about the aerodynamic performance of dense gases flowing at realistic Reynolds-number

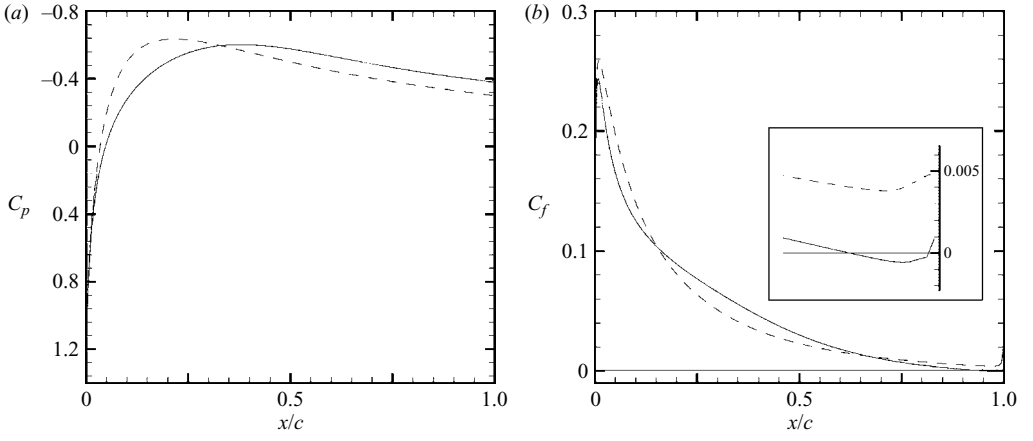

FIGURE 20. Wall distributions of the pressure coefficient and skin friction for laminar flow over a NACA0012 airfoil ($Re = 1000$, $M_\infty = 0.85$). —, perfect gas; - - -, PP10, $p_\infty/p_c = 1.01$, $\rho_\infty/\rho_c = 0.676$.

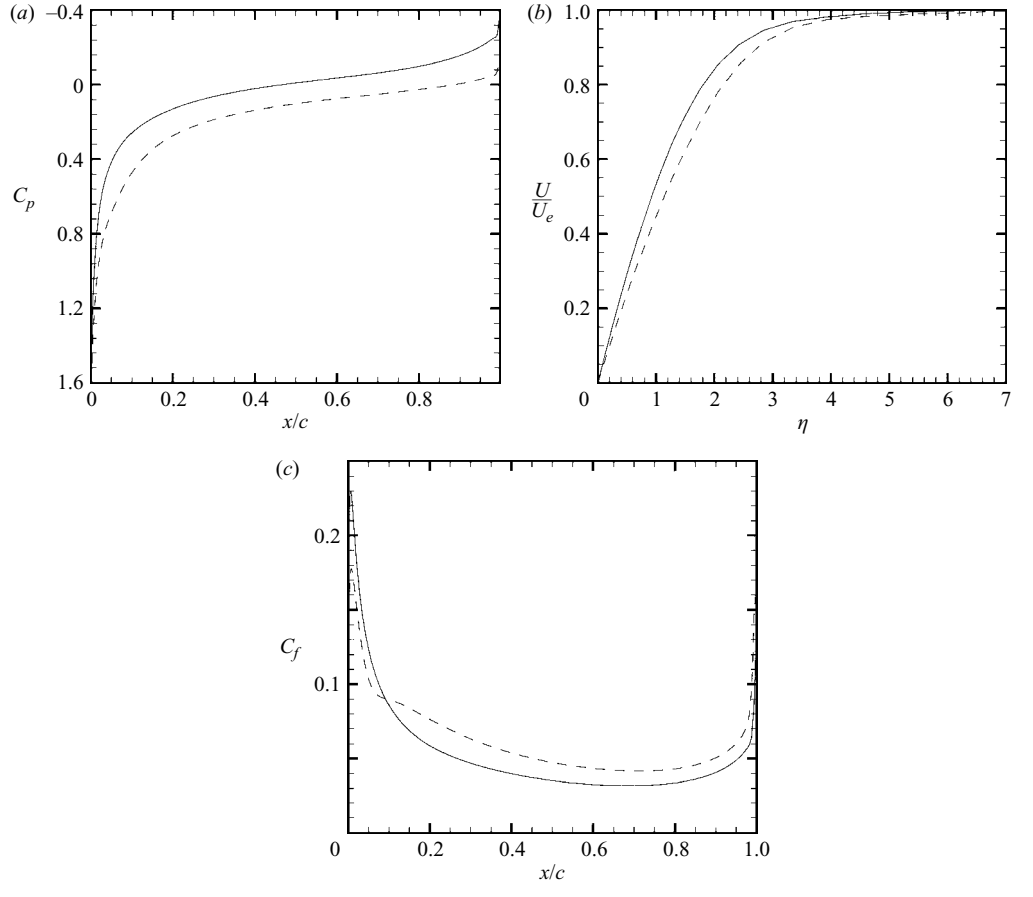

FIGURE 21. Wall distributions of the pressure coefficient and skin friction and velocity profiles at midchord for laminar flow over a NACA0012 airfoil ($Re = 1000$, $M_\infty = 2.0$). $\eta = (y - y_w)/c$ is an adimensional coordinate in the direction normal to the wall. —, PP10; - - -, perfect gas.

conditions. Since typical Reynolds numbers for flows past turbine blades are in the range 10^5–10^6, turbulence effects will be necessarily taken into account. Given the very high flow Reynolds numbers, direct simulations are unfortunately not viable. On the other hand, at this stage, the main objective is to collect information, even if approximate, about how the presence of a thin turbulent boundary layer affects the aerodynamic performance of the system in comparison with results obtained for the previously investigated inviscid case. To this purpose, turbulent DG flows over a flat plate and around an airfoil are investigated, based on the following working hypotheses.

(*a*) Flow conditions are sufficiently far from the thermodynamic critical point that DG effects, such as dramatic variations of the fluid specific heat and compressibility, can be neglected; in these conditions, density fluctuations are not as huge as in near-critical conditions and subsequently the turbulence structure is not affected significantly.

(*b*) At least for equilibrium boundary layers, the mean flow behaviour can be predicted adequately using the compressible Reynolds-averaged Navier–Stokes equations (RANS) completed by an eddy viscosity turbulence model; similarly, the turbulent heat transfer can be modelled though a 'turbulent Fourier law', as usual for PFG flows, where the turbulent thermal conductivity is computed in a classical way by introducing a turbulent Prandtl number, assumed to be roughly constant and $O(1)$ throughout the flow.

Hypothesis (*a*) is justified because the flows of interest for this study because do not evolve in the immediate neighbourhood of the critical point; and in fact, if inviscid analyses and computations show an uncommmon variation of the fluid speed of sound (and hence compressibility) with pressure perturbations, nevertheless the magnitude of these variations is approximately of the order of those occurring in perfect gases. Moreover, peculiar DG phenomena related to flow heating or cooling are excluded from consideration, since the airfoil wall is supposed to be adiabatic. On the contrary, hypothesis (*b*) should be considered with some caution. On the one hand, if hypothesis (*a*) is verified, it seems reasonable to apply to compressible DG flows turbulence models initially developed for incompressible flows of perfect gases and then extended in the common practice to compressible PFG flows; on the other hand, more or less strong pressure gradients and shock waves characterizing the outer inviscid flow are likely to affect the boundary layer, which can no longer be considered an 'equilibrium' one; this is true for PFG flows as well as for DG flows. Thus, aerodynamic performance predictions will necessarily be affected by deficiencies inherent with the chosen turbulence model. Nevertheless, since investigations are intended to provide trends of behaviour more than accurate values of the computed aerodynamic coefficients, use of hypothesis (*b*) represents a means of obtaining preliminary information about realistic DG flows with a reasonable computational expense. Specifically, the present results have been obtained using the simple algebraic model of Baldwin & Lomax (1978), whose deficiencies in non-equilibrium boundary layer are well known (see for example Wilcox 1998, for a wider discussion): for example, flow features such as the location of shock waves and the length of separation bubbles will not be predicted accurately. Nevertheless, it is expected that the model will be able to predict roughly the main trends and qualitative features of the flow field.

Before undertaking the study of complex transonic turbulent flows past an airfoil, turbulent flows over an adiabatic flat plate with zero pressure gradient are considered. For this kind of (equilibrium) boundary layers, the Baldwin–Lomax turbulence model

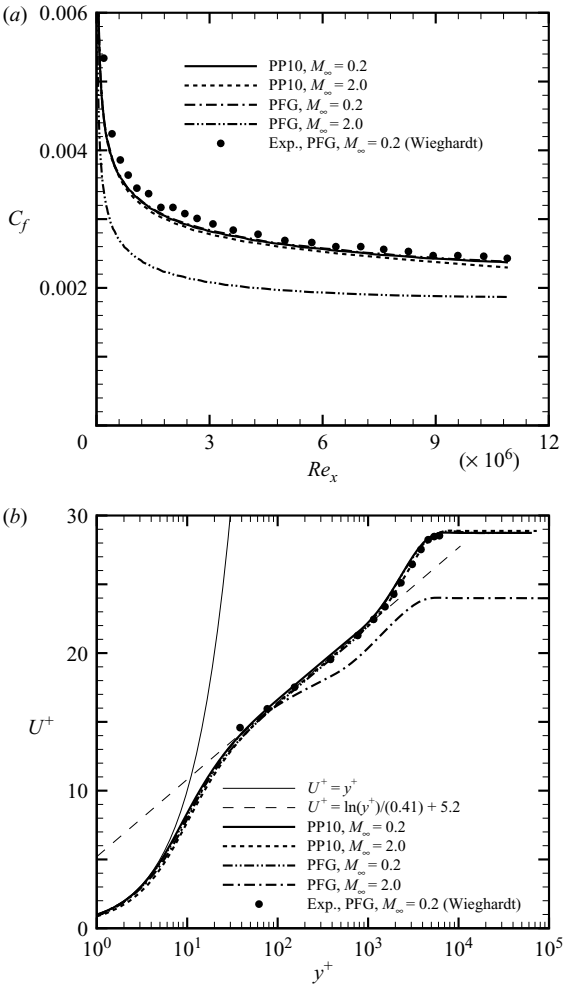

FIGURE 22. Skin friction distribution at the wall and velocity profiles at $Re_x = 1.03 \times 10^7$ for turbulent flows over a flat plate with zero pressure gradient ($Re/L = 660\,000$).

is expected to perform fairly well, which allows us to investigate the basic properties of turbulent DG boundary layers with a higher degree of confidence. Cartesian meshes with 110 cells in the direction tangent to the plate wall and 80 cells in the normal one are used for the study. The grid cells are clustered in the streamwise direction to resolve flow gradients near the leading edge of the plate and normal to the plate to resolve the boundary layer. A series of grids was generated, having y^+ values of 1, 2 and 5 at the first point off the wall. Skin friction distributions on the two grids with finer spacing close to the wall are almost identical. In the following, we discuss results obtained on the finest grid. Figure 22(a) shows skin friction distributions for PFG and DG flows at inlet Mach number equal to 0.2 and 2, respectively. The Reynolds number for unit plate length is 6.6×10^5. For a perfect gas, the skin friction coefficient follows the classical scaling law for turbulent compressible boundary layers, i.e.:

$$\frac{C_f}{C_{f_{inc}}} \propto \left(\frac{\rho_w}{\rho_\infty}\right)^{1/2},$$

where the subscript *inc* refers to the skin friction in incompressible flow, and the subscript w denotes wall quantities. This scaling law can be formulated in terms of the free-stream Mach number and of the recovery factor $r=(T_w-T_\infty)/(U_\infty^2/2\,c_p)=r(Pr)$:

$$\frac{C_f}{C_{f_{inc}}}=\left(1+r\frac{\gamma-1}{4}M_\infty^2\right)^{-1}.$$

A detailed discussion can be found in Schlichting & Gersten (2003). According to this law, we expect $C_f(M_\infty=2)/C_f(M_\infty=0.2)\approx 0.74$; present PFG computations yield a ratio of 0.77. For the dense gas, the scaling law breaks down, and the skin friction distributions at $M_\infty=0.2$ and $M_\infty=2$ are almost superposed to each other and to PFG results at $M_\infty=0.2$. This is confirmed by profiles of the adimensional velocity $u^+:=u/u_\tau$ (with u the streamwise velocity component and $u_\tau=\sqrt{\tau_w/\rho_w}$) versus the viscous-layer coordinate y^+, shown in figure 22(*b*). Both skin friction distributions and velocity profiles at $M_\infty=0.2$ are in good agreement with experimental data of Wieghardt & Tillman (1952).

In order to provide theoretical support for the dense gas results, let us consider the boundary-layer equations in the viscous sublayer close to the wall and in the overlap layer between the viscous wall layer and the fully turbulent outer flow. In both sublayers, the inertial and pressure terms as well as the convective change of the total energy can be neglected, at least for attached boundary layers. We follow hereinafter a similar reasoning to Schlichting & Gersten (2003, pp. 619–620). In the viscous layer, turbulent stresses and heat transport become vanishingly small and the mean velocity and temperature distributions satisfy:

$$\mu\frac{\mathrm{d}u}{\mathrm{d}y}=\tau_w,\quad -\kappa\frac{\mathrm{d}T}{\mathrm{d}y}-u\left(\mu\frac{\mathrm{d}u}{\mathrm{d}y}\right)=q_w. \tag{4.3}$$

Adimensionalizing (4.3) with respect to the reference quantities ρ_w, τ_w, μ_w and T_w, yields:

$$\frac{\mathrm{d}u^+}{\mathrm{d}y^+}=\frac{\mu_w}{\mu},\quad \frac{\mathrm{d}T^+}{\mathrm{d}y^+}=-Pr_w\frac{\kappa_w}{\kappa}(B_q+2Ec_\tau u^+), \tag{4.4}$$

where $T^+=T/T_w$, and $B_q=q_w/(\rho_w u_\tau c_p T_w)$ is the non-dimensional wall heat flux, $Ec_\tau=u_\tau^2/(2c_pT_w)$ is a friction Eckert number and Pr_w is the Prandtl number at the wall, $O(1)$ both for perfect gases and for dense gases far from the immediate vicinity of the critical point. For flows of dense gases, characterized by large specific heats, the friction Eckert number tends to zero. Moreover, $B_q=0$ for adiabatic walls. As a consequence, for flows of dense gases, from (4.4*b*), we find that $T^+=const$ across the viscous sublayer. Therefore, μ and κ are also constant, and integration of the differential equation for u^+ simply gives the universal linear law:

$$u^+=y^+.$$

In the overlap layer, i.e. the outer part of the wall layer in which the effects of molecular viscosity and thermal conductivity can already be neglected, the following relationships hold (see Schlichting & Gersten 2003, p. 620):

$$\tau_t=\tau_w,\quad q_t=q_w+u\tau_t, \tag{4.5}$$

where τ_t is the turbulent shear stress and q_t the turbulent heat flux. These quantities are currently modelled by introducing an eddy viscosity μ_t and an eddy thermal

conductivity κ_t:

$$\tau_t = \mu_t \frac{\mathrm{d}u}{\mathrm{d}y}, \quad q_t = -\kappa_t \frac{\mathrm{d}T}{\mathrm{d}y}.$$

Injecting these expressions into (4.5) and combining them both yields the following differential equation:

$$\frac{\mathrm{d}T}{\mathrm{d}u} = -Pr_t \frac{q_w + u\tau_w}{c_p \tau_w}, \tag{4.6}$$

where $Pr_t = c_p \mu_t / \kappa_t$ is the turbulent Prandtl number, supposed constant and $O(1)$ throughout the flow. The preceding equation can also be written in adimensional form:

$$\frac{\mathrm{d}T^+}{\mathrm{d}u^+} = -Pr_t(B_q + 2Ec_\tau u^+), \tag{4.7}$$

which, for adiabatic flows with vanishingly small Eckert number, gives again:

$$T^+ \approx const$$

across the overlap layer. On the other hand, classical similarity considerations for the velocity gradient deliver:

$$\frac{\mathrm{d}u}{\mathrm{d}y} = \sqrt{\frac{\tau_w}{\rho}} \frac{1}{k\,y} = \frac{u_\tau}{k\,y} \sqrt{\frac{\rho_w}{\rho}}, \tag{4.8}$$

with k the von Kármán constant. Since for flows with $Ec_\tau \to 0$, both temperature and pressure remain constant across the overlap layer, this must also be true for the density, and the term inside the square root is substantially equal to 1. As a consequence, integration of (4.8) yields:

$$u^+ = \frac{u}{u_\tau} = \frac{1}{k} \ln y^+ + C_2, \tag{4.9}$$

just as in incompressible flows, and in agreement with the preceding numerical results. For incompressible boundary layers, experiments deliver $k = 0.41$ and $C_2 = 5$. Theoretical curves for the velocity variation inside the viscous and the overlap layers are reported in figure 22(*b*) for reference.

We now turn to transonic flows over an airfoil at $M_\infty = 0.85$, $\alpha = 1°$, and $Re = 9 \times 10^6$. A parametric study is performed for a series of operation points lying on isentrope S4 (see figure 4). Solutions are computed using C-grids of 256×64 and 256×128 cells, as discussed in § 3. Assuming a (conservative) value of the convergence order equal to 1.8 for the scheme extended to viscous flows, the computed GCI turns out to be about 0.5 % on the finer grid (retained for all computations presented hereinafter).

The reference solution for a diatomic perfect gas flowing at the same conditions is represented in figure 23(*a*). The flow is characterized by strong shock waves at both airfoil surfaces, which interact with the turbulent boundary layer. At the upper surface, an extended post-shock separation bubble appears. The aerodynamic coefficients are $C_d = 5.28 \times 10^{-2}$ and $C_l = -0.012$, the negative sign being due to significant upstream displacement of the upper shock owing to flow separation. Wall distributions of the pressure coefficient for viscous and inviscid flow are displayed in figure 23(*b*). The computed values of the aerodynamic coefficients for PP10 at various operating conditions are reported in figure 25. If the free-stream state is taken close enough to the inversion zone, the flow remains subsonic: no shock waves are formed and flow separation is suppressed. In this regime (subcritical BZT regime), wave drag disappears and the drag coefficient drops from its PFG value, whereas

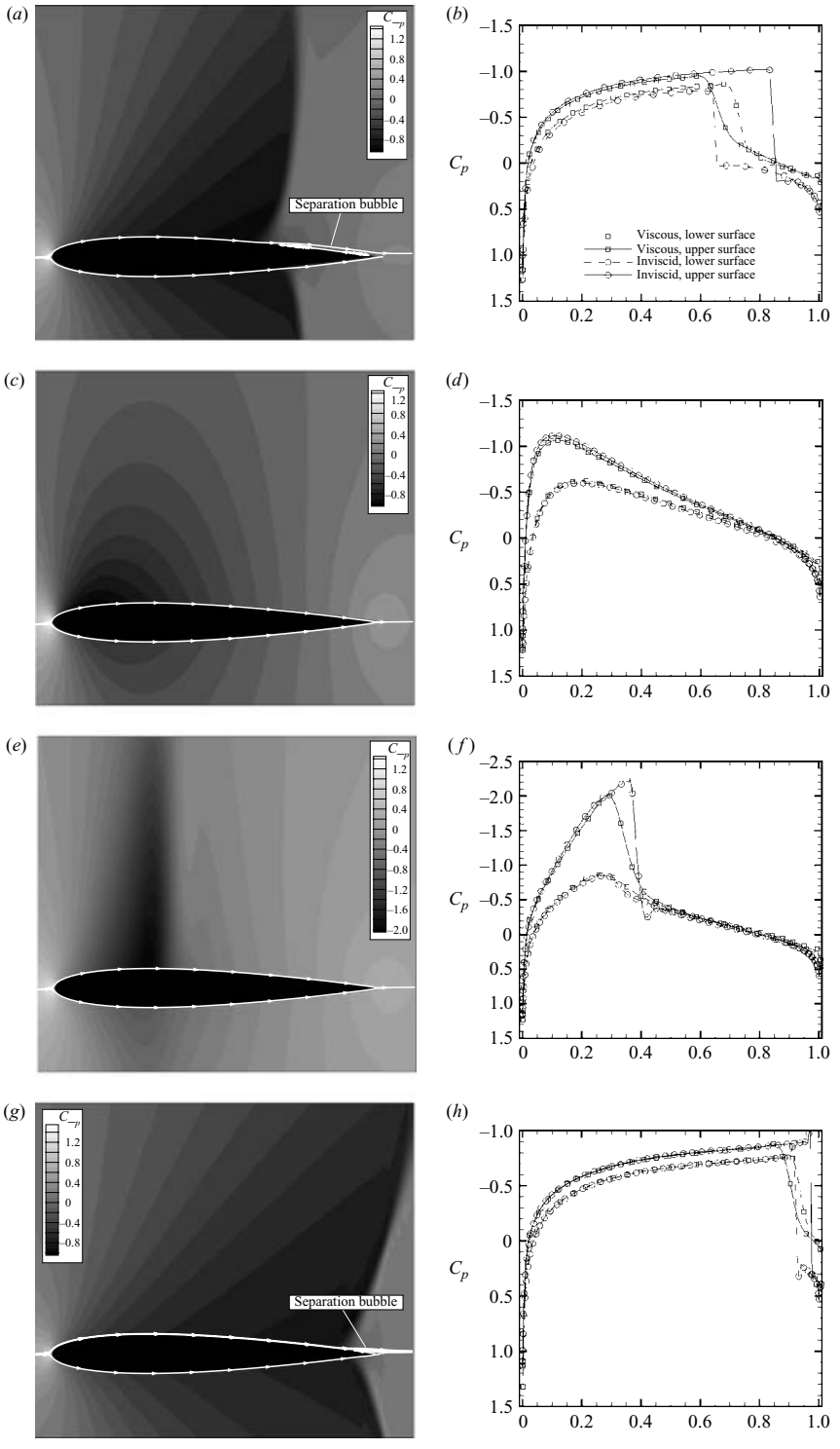

FIGURE 23. Turbulent flow over the NACA0012 airfoil, $M_\infty = 0.85$, $\alpha = 1^\circ$, $Re = 9 \times 10^6$. Pressure coefficient contours and streamlines (left) and wall pressure coefficient (right) for a perfect gas flow (a, b) and for PP10 at operating conditions $p_\infty/p_c = 1.01$, $\rho_\infty/\rho_c = 0.676$ (c, d), $p_\infty/p_c = 1.08$, $\rho_\infty/\rho_c = 0.850$ (e, f), $p_\infty/p_c = 1.17$, $\rho_\infty/\rho_c = 1.11$ (g, h).

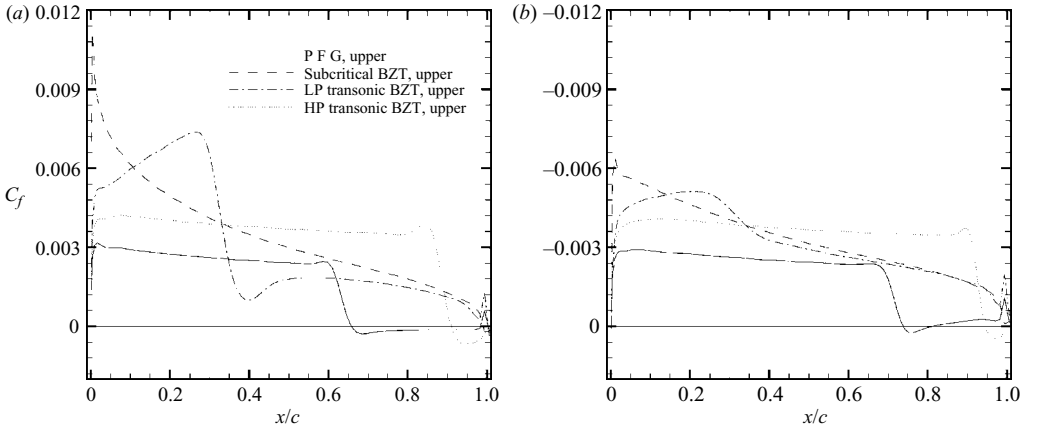

FIGURE 24. Skin friction for a perfect gas flow and dense gas flows at different operating conditions.

the lift coefficient is considerably higher. For operation points at higher free-stream Γ, in the regime previously called 'low-pressure transonic BZT', a supersonic region forms. This enhances lift, whereas wave drag remains low with respect to the perfect gas case. Two mechanisms contribute to this effect: the first is of an inviscid nature, and is related to shock waves having jump conditions in the neighbourhood of the transition line, and therefore being less dissipative than normal; on the other hand, such weak shock waves do not cause flow separation, so that pressure drag is further reduced. Further increasing the free-stream pressure (high-pressure transonic BZT regime), shock waves become stronger and the flow finally separates because of shock/boundary-layer interactions. Accordingly, both the lift coefficient and the lift-to-drag ratio drop down. Figure 23(c, e, g) shows typical pressure coefficient contours and flow streamlines in the three regimes; wall distributions of the pressure coefficient for inviscid and viscous flow are shown in figure 23(d, f, h). Figure 24 compares skin friction distributions for a perfect gas and for PP10 at different operating conditions. Extended separated regions characterize the perfect gas flow at both airfoil surfaces, whereas dense gas flows remain attached insofar as the operating conditions are sufficiently close to the inversion zone. In the subcritical case, for flows at high Reynolds number, the pressure distribution remains essentially similar to the inviscid one, with just some smoothing of the suction peaks at both surfaces downstream of the leading edge. The lift coefficient is slightly below the inviscid value, whereas the lift-to-drag ratio now takes, of course, finite, although high values. In the low-pressure transonic BZT regime, the differences become more significant. Namely, the suction peak at the airfoil upper surface is dramatically smoothed out because of viscous effects, and the location of the upper shock wave moves upstream because of interactions with the boundary layer: nevertheless, the flow remains attached. Also note that in this regime, the skin friction (see figure 24) significantly grows with chordwise distance up to $x/c \approx 0.25$, owing to the strong favourable pressure gradient acting on the boundary layer. Finally, in the third regime, strong shock/boundary-layer interactions lead to flow separation at both airfoil surfaces: nonetheless, separation is delayed and separated regions are smaller than in perfect gas flow. In summary, results suggest that DG effects mainly affect the inviscid

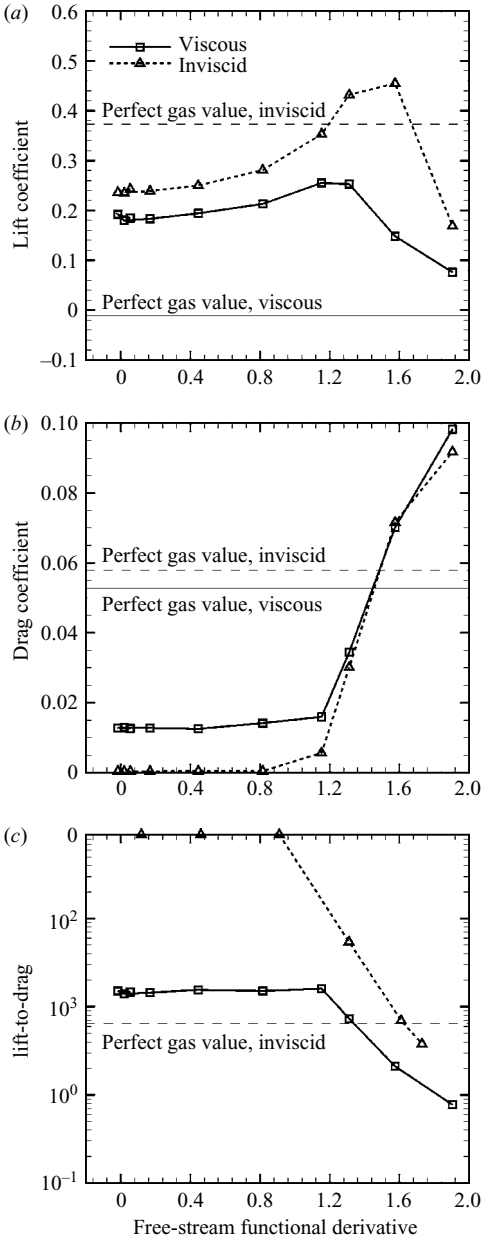

FIGURE 25. Aerodynamic coefficients versus free-stream fundamental derivative for turbulent flows at $M_\infty = 0.85$, $\alpha = 1^\circ$ and $Re = 9 \times 10^6$ past a NACA0012.

flow behaviour, whereas the viscous behaviour is influenced indirectly according to the distributions of the external pressure and Mach number characterizing flows at different operating conditions. Concerning system efficiency, the use of dense gases working at proper operating conditions has a definitely beneficial effect, not only because of significant reductions in wave drag, but also because losses due to shock/boundary-layer interaction are completely suppressed or strongly attenuated.

5. Conclusions

In the present work, a careful numerical investigation of a number of inviscid, viscous laminar and viscous turbulent flows of a dense gas over an airfoil at transonic speeds has been undertaken. The numerical results provide a complete picture of the complex aerodynamics of an airfoil immersed in a dense gas stream. Inviscid mechanisms include non-monotonic variation of the Mach number with density, leading to increases in the critical Mach number and in a delay of the transonic drag rise, and the appearance of weak non-classical waves with jump conditions in the vicinity of the transition line, which may lead to significant improvements in the airfoil aerodynamic performance over a classical working fluid. For flows with high-subsonic free-stream, analyses of the variation of aerodynamic coefficients with free-stream thermodynamic conditions allow us to identify three flow regimes in the range of thermodynamic conditions swept in the present calculations, representative of the operating range of an organic Rankine cycle turbine. While the drag always increases with free-stream pressure and fundamental derivative Γ, the lift coefficient displays an optimum in the second regime, referred to as a low-pressure transonic BZT regime in the present study, and then drops dramatically. The lift-to-drag ratio is poor for high Γ_∞ flows, but tends to infinity as the free-stream value of Γ approaches unity from the high-pressure side of the inversion zone. The best compromise solution between high lift and low drag is obtained in the second regime, for Γ_∞ approximately in the range 1–1.3: in these conditions, higher lift and significantly reduced wave drag compared to perfect gas results is observed.

For sonic and (all the more so) low supersonic conditions, efficiency gains over classical working fluids are less impressive with respect to the previous case. However, for all inviscid computations performed in this study, the best trade-off between high lift and aerodynamic efficiency is obtained for operation points relatively far from the inversion zone, that is, for flows with Γ_∞ of the order of unity. Such results are important for practical applications; in particular, it seems possible to overcome one of the major difficulties for the development of BZT organic Rankine cycles, namely, the necessity of operating the turbine inside the inversion zone. Present results indicate that, in practice, significant performance enhancement can be achieved by operating the system within the thermodynamic region where $\Gamma < 1$. In order to obtain the maximum benefit from the use of BZT working fluids, it is nevertheless important to operate the system at transonic speeds, since the aerodynamic performance drops quickly as the free-stream Mach number increases.

Numerical studies of the aerodynamic behaviour of viscous dense gas flows past an airfoil have also been provided for the first time, to our knowledge. For laminar flows, dense gas effects in the outer inviscid flow region delay boundary-layer separation. Moreover, at sufficiently large Mach numbers, further benefits derive from reduced friction heating in flows of gases with large specific heats, such as BZT gases. Theoretical as well as numerical results for an adiabatic flat plate presented here for the first time show that reduced sensitivity to friction heating also characterizes turbulent boundary-layer flows of dense gases.

Beneficial effects deriving from the use of a dense working fluid are also observed when the aerodynamic performance of viscous turbulent airfoil flows at large Reynolds number and transonic speeds is considered. The non-classical variation of the Mach number with density favourably affects the boundary-layer development, contributes to reducing friction drag and to avoiding boundary-layer separation. Specifically, post-shock separations due to shock/boundary-layer interaction are suppressed or greatly reduced, which ensures satisfactory lift and aerodynamic efficiency at flow

conditions where the aerodynamic performance of perfect gas flows suffers from huge post-shock separation.

As a final consideration, note that present results have been obtained for a specific airfoil shape, and that efficiency gains are only due to the peculiar properties of the working fluid; the use of modern multi-point optimization techniques could allow the selection of airfoil shapes with even higher aerodynamic performances over a larger operation range. For example, the study presented in Congedo, Corre & Cinnella (2007) shows that shape optimization allows simultaneous increase the lift in the subcritical BZT regime and minimization of the drag for a given level of lift in the supercritical regimes, futher delaying the transonic drag rise and enlarging the system operation range.

REFERENCES

Baldwin, B. & Lomax, H. 1978 Thin layer approximation and algebraic model for separated turbulent flows. *AIAA Paper* 78–257.

Brown, B. P. & Argrow, B. M. 2000 Application of Bethe–Zel'dovich–Thompson in organic Rankine cycles. *J. Prop. Power* **16**, 1118–1124.

Cengel, Y. A. & Boles, M. A. 2006 *Thermodynamics: an Engineering Approach*, 5th edn. McGraw-Hill.

Chung, T. H., Ajlan, M., Lee, L. L. & Starling, K. E. 1988 Generalized multiparameter correlation for nonpolar and polar fluid transport properties. *Ind. Engng Chem. Res.* **27**, 671–679.

Cinnella, P. & Congedo, P. M. 2005*a* Aerodynamic performance of transonic Bethe–Zel'dovich–Thompson flows past an airfoil. *AIAA J.* **43**, 370–378.

Cinnella, P. & Congedo, P. M. 2005*b* Numerical solver for dense gas flows. *AIAA J.* **43**, 2457–2461.

Congedo, P. M., Corre, C. & Cinnella, P. 2007 Airfoil shape optimization for transonic flows of Bethe–Zel'dovich–Thompson fluids. *AIAA J.* **5** (in press).

Cramer, M. S. 1989*a* Negative nonlinearity in selected fluorocarbons. *Phys. Fluids* A **1**, 1894–1897.

Cramer, M. S. 1989*b* Shock splitting in single-phase gases. *J. Fluid Mech.* **199**, 281–296.

Cramer, M. S. 1991 Nonclassical dynamics of classical gases. In *Nonlinear Waves in Real Fluids* (ed. A. Kluwick), pp. 91–145. Springer.

Cramer, M. S. & Crickenberg, A. B. 1991 The dissipative structure of shock waves in dense gases. *J. Fluid Mech* **223**, 325–355.

Cramer, M. S. & Kluwick, A. 1984 On the propagation of waves exhibiting both positive and negative nonlinearity. *J. Fluid Mech.* **142**, 9–37.

Cramer, M. S. & Park, S. 1999 On the suppression of shock-induced separation in Bethe–Zel'dovich–Thompson fluids. *J. Fluid Mech* **393**, 1–21.

Cramer, M. S. & Tarkenton, G. M. 1992 Transonic flows of Bethe–Zel'dovich–Thompson fluids. *J. Fluid Mech.* **240**, 197–298.

Cramer, M. S., Whitlock, S. T. & Tarkenton, G. M. 1996 Transonic and boundary layer similarity laws in dense gases. *Trans. ASME* I: *J. Fluids Engng* **118**, 481–485.

Dervieux, A., van Leer, B. & Rizzi, A. (ed.) 1989 *Numerical Simulation of Compressible Euler Flows*, *Notes on Numerical Fluid Mechanics*, vol. 26. Vieweg.

Emanuel, G. 1994 Assessment of the Martin–Hou equation for modelling a nonclassical fluid. *Trans. ASME* I: *J. Fluids Engng* **116**, 883–884.

Guardone, A., Vigevano, L. & Argrow, B. M. 2004 Assessment of themodynamic models for dense gas dynamics. *Phys. Fluids* **16**, 3878–3887.

Hayes, W. D. 1966 La seconde approximation pour les écoulements transsoniques non visqueux. *J. Méc.* **5**, 163–206.

Jameson, A., Schmidt, W. & Turkel, E. 1981 Solutions of the Euler equations by finite volume methods using Runge–Kutta time stepping schemes. *AIAA Paper* 81-1259.

Kluwick, A. 2000 Marginally separated flows in dilute and dense gases. *Phil. Trans. R. Soc. Lond.* A **358**, 3169–3192.

Kluwick, A. 2004 Internal flows of dense gases. *Acta Mech.* **169**, 123–143.

Kluwick, A. & Wrabel, M. 2004 Shock boundary layer interactions in dense gases. *PAMM* **4**, 444–445.

Lambrakis, K. C. & Thompson, P. A. 1972 Existence of real fluids with a negative fundamental derivative γ. *Phys. Fluids* **15**, 933–935.

Martin, J. J. & Hou, Y. C. 1955 Development of an equation of state for gases. *AIChE J.* **1**, 142–151.

Monaco, J. F., Cramer, M. S. & Watson, L. T. 1997 Supersonic flows of dense gases in cascade configurations. *J. Fluid Mech.* **330**, 31–59.

Morren, S. H. 1991 Transonic aerodynamics of dense gases. Master's thesis, Engineering Science and Mechanics Department, Virginia Polytechnic Institute and State University, also appeared as *NASA TM* 103732.

Reid, R. C., Prausnitz, J. M. & Poling, B. E. 1987 *The Properties of Gases and Liquids*, 4th edn. McGraw-Hill.

Rezgui, A., Cinnella, P. & Lerat, A. 2001 Third-order accurate finite volume schemes for Euler computations on curvilinear meshes. *Computers Fluids* **30**, 875–901.

Roache, P. J. 1998 *Verification and Validation in Computational Science and Engineering*. Hermosa, Albuquerque, New Mexico.

Rusak, Z. & Wang, C. W. 1997 Transonic flow of dense gases around an airfoil with a parabolic nose. *J. Fluid Mech.* **346**, 1–21.

Schlichting, H. & Gersten, K. 2003 *Boundary Layer Theory*, 8th edn. Springer.

Thompson, P. A. 1971 A fundamental derivative in gas dynamics. *Phys. Fluids* **14**, 1843–1849.

Thompson, P. A. & Lambrakis, K. C. 1973 Negative shock waves. *J. Fluid Mech.* **60**, 187–208.

Wang, C. W. & Rusak, Z. 1999 Numerical studies of transonic BZT gas flows around thin airfoils. *J. Fluid Mech* **396**, 109–141.

Wieghardt, K. & Tillman, W. 1952 On the turbulent friction layer for rising pressure. *NACA TM* 1314.

Wilcox, D. C. 1998 *Turbulence modeling for CFD*, 2nd edn. DCW Industries.